Received 7 June 2021; accepted 26 June 2021. Date of publication 6 July 2021; date of current version 18 August 2021.

Digital Object Identifier 10.1109/OJCOMS.2021.3094927

Zero-Crossing Modulation for Wideband Systems Employing 1-Bit Quantization and Temporal Oversampling: Transceiver Design and Performance Evaluation

PETER NEUHAUS (Graduate Student Member, IEEE), MEIK DÖRPINGHAUS (Member, IEEE), AND GERHARD FETTWEIS (Fellow, IEEE)

Vodafone Chair Mobile Communications Systems, Technische Universität Dresden, 01062 Dresden, Germany

CORRESPONDING AUTHOR: P. NEUHAUS (e-mail: peter_friedrich.neuhaus@tu-dresden.de)

This work was supported in part by Nokia Bell Labs, Stuttgart, Germany; in part by the Deutsche Forschungsgemeinschaft (DFG, German Research Foundation) under Project 164481002—SFB 912, HAEC; and in part by the German Federal Ministry of Education and Research (BMBF) through Project E4C under Contract 16ME0189. This work has been presented in part at the 2020 IEEE International Conference on Communications, Dublin, Ireland, [1] and in part at the 2020 IEEE International Symposium on Personal, Indoor and Mobile Radio Communications, London, U.K. [2].

ABSTRACT Next-generation wireless communications systems are anticipated to utilize the vast amount of available spectrum in the millimeter-wave and sub-terahertz bands above 100 GHz to meet the ever-increasing demand for higher data rates. However, the analog-to-digital converter (ADC) power consumption is expected to be a major bottleneck if conventional system designs are employed at these frequencies. Instead, shifting the ADC resolution from the amplitude domain to the time domain by employing 1-bit quantization and temporal oversampling w.r.t. the Nyquist rate is expected to be more energy-efficient. Hence, we consider a system employing 1-bit quantization and temporal oversampling at the receiver, which operates on a wideband line-of-sight channel. We present a practical transceiver design for a zero-crossing modulation waveform, which combines faster-than-Nyquist signaling and runlength-limited (RLL) transmit sequences. To this aim, we derive four fixed-length finite-state machine RLL encoders enabling efficient transmit signal construction and soft-demapping at the receiver. Moreover, we propose a soft-output equalizer, which approximates maximum a posteriori RLL symbol detection. We evaluate the system performance in terms of peak-to-average-power ratio, coded block error rate, and a lower bound on the spectral efficiency (SE) w.r.t. a fractional power containment bandwidth. Our numerical results show that SEs of up to 4 bit/s/Hz are achievable with the presented transceiver design.

INDEX TERMS 1-bit, quantization, oversampling, runlength-limited sequences, faster-than-Nyquist signaling, equalization.

I. INTRODUCTION

FUTURE wireless communications systems are envisioned to provide data rates in the order of 100 Gbit/s and above by utilizing the sizeable amount of free spectrum in the millimeter-wave (mmWave) and sub-terahertz (THz) bands [3]. At those frequencies, it is necessary to employ highly directional antenna arrays at both, the transmitter and the receiver because the *isotropic* path loss increases inversely with the wavelength squared due to *Friis' Law* [4]. The analog-to-digital converter (ADC) power consumption of such systems is expected to be a significant design challenge: Employing one radio frequency (RF) chain per antenna element, which is typically the case in conventional sub-6 GHz multiple-input multiple-output (MIMO) systems, would result in a large number of ADCs. Furthermore, empirical results show that the ADC power consumption grows quadratically with the input bandwidth for bandwidths above approx. 300 MHz [5], which is expected to result in a

significantly increased ADC power consumption compared to today's systems.

Hence, analog or hybrid analog-digital beamforming architectures are proposed for mmWave and sub-THz systems to reduce the number of ADCs [4]. Moreover, a widely proposed approach to decrease the power consumption of each individual ADC is to reduce the amplitude resolution because the power consumption grows exponentially with the amplitude resolution measured in bits [6]. Employing 1-bit quantization is especially promising, as it is anticipated to allow for relaxed linearity requirements of the analog front end, e. g., it might be possible to operate the baseband amplifiers in saturation.

Simultaneously, the *time-domain* resolution is becoming superior to the *amplitude-domain* resolution in nanometer-scale CMOS processes [7], [8]. This is caused, on the one hand, by improved switching capabilities and, on the other hand, by reduced supply-voltages leaving less voltage headroom for processing in the amplitude domain. Consequently, it is foreseen to be more energy-efficient to shift the resolution from the amplitude to the time domain, i.e., by employing 1-bit quantization and temporal oversampling.

In [9], it has been shown that oversampling the output of a 1-bit quantizer can increase the information rate beyond 1 bit per Nyquist interval when considering the noiseless case. Again studying the noiseless case, it has been proven in [10] that information rates of $\log_2(1 + M_{\mathrm{Rx}})$ bit per Nyquist interval are achievable by M_{Rx}-fold oversampling with respect to (w.r.t.) the Nyquist rate. This rate is achieved by constructing bandlimited transmit signals with predefined zero-crossing patterns, which encode the information. Furthermore, in [11] and [12], it has been shown that for an additive white Gaussian noise (AWGN) channel, oversampling can improve the performance in terms of capacity per unit-cost and generalized mutual information, respectively. Bounds on the achievable rate for a bandlimited 1-bit quantized continuous-time AWGN channel have been investigated in [13], [14]. The continuous-time channel studied therein corresponds to the limiting case of infinite oversampling. From [9]–[14], it is essential to understand that: *i*) oversampling w. r. t. the Nyquist rate can recover some of the loss due to 1-bit quantization (in contrast to systems with infinite amplitude resolution, where Nyquist rate sampling is sufficient), and *ii*) the information is effectively conveyed in the *temporal distance* between zero-crossings because all magnitude information is lost after 1-bit quantization.

Hence, in [15], it has been stated that for systems employing 1-bit quantization and temporal oversampling, the information should be encoded in the distance between zero-crossings, a concept denoted as zero-crossing modulation (ZXM). In [16], several ZXM schemes have been compared w. r. t. numerically computed lower bounds on the spectral efficiency (SE) for an AWGN channel. Therein, the modulation proposed in [17], i.e., using a transmit signal design based on the combination of faster-than-Nyquist (FTN) signaling [18] and runlength-limited (RLL) [19] transmit sequences is found to yield the highest SE among the considered modulations. Intuitively, this modulation is a good match for the considered system because it results in some kind of symmetry between the transmitter and the receiver: On each component, i.e., the in-phase and quadrature component, the transmitter employs binary antipodal signaling at a rate exceeding the Nyquist rate, whereas the receiver employs 1-bit quantization and temporal oversampling. Similarly, the works [20]–[22] also investigate SE lower bounds for different ZXM schemes over AWGN channels. However, none of the works [16], [17], [20]–[22] considers a practical transceiver design, i.e., they neither consider mapping bits onto the waveform at the transmitter nor a detector implementation at the receiver.

Recently, practical implementations of systems employing 1-bit quantization and oversampling at the receiver have been proposed and evaluated: A multi-user massive MIMO downlink system, where the receivers employ 1-bit quantization and temporal oversampling, has been studied in [23]. The authors propose a *quantization precoder* which optimizes the transmit signal under a bandwidth constraint, such that the payload bits can be uniquely detected from the 1-bit quantized observations at the receiver in the absence of noise. Spatio-temporal precoding for a similar setup as in [23] has been considered in [24], [25], where the authors also proposed a superior bit-mapping, denoted as *zero-crossing precoding*. The benefits of employing temporal oversampling in a massive MIMO uplink scenario with 1-bit ADCs have been illustrated in [26]. Based on the transmit signal design from [10], the authors of [27] have recently proposed and evaluated a practical transceiver design. Notably, they showed that similar rates, as obtained for the noiseless case in [10], can be achieved by their implementation over noisy channels at high signal-to-noise ratio (SNR). Two soft-output detection algorithms for mmWave MIMO systems employing low-resolution ADCs have been proposed in [28].

In this work, we present a transceiver design of a bit-interleaved coded modulation (BICM) [29], [30] system employing ZXM, which is implemented by combining FTN signaling with RLL transmit sequences, as proposed in [16], [17]. The considered single-carrier modulation is well suited for the targeted mmWave and sub-THz frequency bands [31]. Furthermore, in contrast to the prior works [16], [17], [20]–[22], we consider a practical transceiver implementation including modulation, equalization, and soft-demodulation, i.e., we consider end-to-end data transmission. The proposed transceiver design is tailored to a wideband line-of-sight (LOS) channel model including the spatial-wideband effect (SWE) [32], which is caused by propagation delays across the receiver antenna array. The LOS channel model is justified by the fact that the effective channel after beam alignment typically contains only a

single dominant path [33]. For simplicity, we omit transmit beamforming in this work.

Our main contributions are summarized as follows:

- We derive four fixed-length finite-state machine (FSM) RLL codes for efficient transmit signal construction and trellis-based soft-demapping. All derived codes achieve an encoding efficiency of more than 90 % compared to ideal maximum entropy RLL sequences.
- A *soft-output* equalizer implementation is presented, which approximates maximum a posteriori (MAP) RLL symbol detection, and allows to obtain soft-information at the receiver despite employing 1-bit quantization.
- We investigate the complexity of the presented receiver, i.e., of the soft-output equalizer and the soft-input soft-output (SISO) RLL decoder. A comparison shows that the main complexity is due to the equalizer.
- A lower bound on the system's SE w. r. t. a fractional power containment bandwidth is derived. The bound is obtained by lower-bounding the mutual information between bits at the RLL encoder input and the corresponding log-likelihood ratios (LLRs) obtained at the RLL decoder output.
- Finally, we provide a comprehensive numerical performance evaluation of the considered system: For typical configurations, the peak-to-average power ratio (PAPR) is found to be up to 1.5 dB lower when compared to conventional phase-shift keying (PSK) systems. Our numerical evaluation of the derived SE lower bound demonstrates that SEs of up to 4 bit/s/Hz are achievable with the presented transceiver design at sufficiently high SNR when allowing for 5 % out-of-band (OOB) emissions. Furthermore, we compare the SE of the presented transceiver design to previously obtained lower bounds when employing maximum entropy RLL sequences, to an unquantized 8-PSK system, and to the related system from [27], which also employs 1-bit quantization and temporal oversampling. We find that the presented system significantly outperforms the system from [27] for all considered configurations. A block error rate (BLER) performance evaluation when employing a 5G NR low-density parity-check (LDPC) code [34] shows that a goodput of up to 3.5 bit/s/Hz is feasible when allowing for 5 % OOB emissions. Finally, we investigate the impact of the SWE when implementing low-cost narrowband analog combining using a phase shifter network (PSN). Our results indicate that the loss due to narrowband beamforming is small for many practical combinations of antenna array size and bandwidth-to-carrier-frequency ratio.

Compared to our previous works [1] and [2], we derive two additional FSM RLL codes, thereby extending the evaluation to higher FTN signaling and oversampling factors, which enables higher SEs. Moreover, we extend the modeling of intersymbol interference (ISI) in the system model, present an improved SE lower bound, and evaluate the complexity of the presented receiver. In addition, the numerical evaluation is extended by an investigation of the PAPR, the goodput, and a comparison to previously obtained lower bounds when considering maximum entropy RLL sequences.

The remainder of this work is organized as follows: First, in Section II, we briefly review FTN signaling and maximum entropy RLL sequences, which are combined to implement ZXM. Second, in Section III, we introduce the system model. Afterwards, our main contributions are detailed in Section IV and Section V, which contain the proposed transceiver design and a derivation of a SE lower bound, respectively. Subsequently, we provide a comprehensive numerical performance evaluation of the presented system in Section VI. Finally, our work is concluded in Section VII.

Notation: Vectors and matrices are written as boldface lower and upper case letters, e. g., $\mathbf{x}$ and $\mathbf{X}$, respectively. We use the shorthand notations $\mathbf{x}^m = [x_1, \ldots, x_m]^T$ and $\mathbf{x}_k^m = [x_k, \ldots, x_m]^T$, with $k < m$ and $k, m \in \mathbb{N}$. Random quantities are denoted by sans serif letters, e.g., x, whereas x represents a deterministic quantity. The identity matrix of size $N \times N$ is written as $\mathbf{I}_N$, and the all-zero vector of length N is written as $\mathbf{0}_N$. Finite sets are denoted by upper case calligraphic letters, e. g., $\mathcal{A}$. We use j, $*$, $\mathbb{E}\{\cdot\}$, $\Re\{\cdot\}$ and $\Im\{\cdot\}$ to denote the imaginary unit, convolution, stochastic expectation, the real part, and the imaginary part, respectively. $|\cdot|$ represents the absolute value if the argument is a scalar, i.e., $|x|$, it denotes the determinant if the argument is a matrix, i.e., $|\mathbf{X}|$, and it represents the cardinality if the argument is a set, i.e., $|\mathcal{X}|$. $\lfloor\cdot\rfloor$ denotes rounding to the next smaller integer, while $\mathrm{mod}(a, b)$ represents the remainder of the division $\frac{a}{b}$. The sets of natural, integer, real, and complex numbers are written as $\mathbb{N}$, $\mathbb{Z}$, $\mathbb{R}$, and $\mathbb{C}$, respectively.

II. REVIEW OF ZERO-CROSSING MODULATION

In this section, we briefly review ZXM, which is specifically designed for systems employing 1-bit quantization and temporal oversampling at the receiver. The concept has been studied in [15]. The underlying idea is to encode the information in the *temporal distance* between zero-crossings, as all magnitude information is lost after 1-bit quantization. One implementation method of ZXM is to combine FTN signaling with RLL transmit sequences, as first proposed in [16], [17].

A. FASTER-THAN-NYQUIST SIGNALING

Employing FTN signaling allows to increase the temporal resolution at the transmitter by reducing the temporal distance between transmit symbols [18]. More specifically, in this work, we transmit M_{Tx} symbols per Nyquist interval T_{N}, i.e., the signaling rate is $\frac{M_{\mathrm{Tx}}}{T_{\mathrm{N}}}$. Note that $M_{\mathrm{Tx}} = 1$ corresponds to conventional Nyquist rate signaling. Employing FTN signaling allows to create zero-crossings on a fine grid, hence, allowing to increase the achievable rate [16], [17]. However,

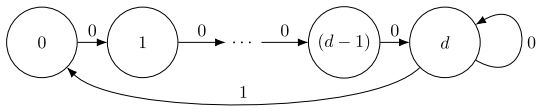

FIGURE 1. Illustration of the $(d, k = \infty)$ constraint as finite-state machine.

it comes at the cost of self-introduced ISI. In the considered ZXM implementation, the amount of ISI is reduced by utilizing RLL transmit sequences.

B. RUNLENGTH-LIMITED SEQUENCES

RLL sequences are typically constructed from so-called (d, k) sequences, which are binary sequences with two constraints: Between every '1' in the sequence, there have to be at *least* d '0's and at *most* k '0's, with $0 \leq d \leq k \leq \infty$. An illustration of this constraint is provided in Fig. 1. RLL sequences are constructed form (d, k) sequences by non-return-to-zero-inverse (NRZI) encoding, where every '1' in the (d, k) sequence results in an amplitude transition in the corresponding RLL sequence [35]. This is illustrated in the following example for $(d = 1, k = \infty)$:

$$\begin{aligned} (d,k)\text{ seq.} \quad & \tilde{\mathbf{a}}^m = [\ldots, \ 0, \ 1, \ 0, \ 0, \ 1, \ 0, \ 1, \ldots] \\ \text{RLL seq.} \quad & \mathbf{a}^m = [\ldots, -1, \ 1, \ 1, \ 1, -1, -1, \ 1, \ldots], \end{aligned}$$

where $m \in \mathbb{N}$ denotes the length of the sequence. In ZXM, the d constraint allows controlling the minimum distance between zero-crossings, which determines the amount of ISI. In the remainder of this work, we omit the k constraint, i.e., we set $k = \infty$, which maximizes the entropy.

RLL sequences are completely defined by the directed adjacency matrix, which describes the underlying FSM (cf. Fig. 1). For $k = \infty$, the adjacency matrix, denoted by $\mathbf{A}_d$, is of size $(d + 1) \times (d + 1)$. Examples for $d = 1$ and $d = 2$ are

$$\mathbf{A}_{d=1} = \begin{bmatrix} 0 & 1 \\ 1 & 1 \end{bmatrix}, \quad \mathbf{A}_{d=2} = \begin{bmatrix} 0 & 1 & 0 \\ 0 & 0 & 1 \\ 1 & 0 & 1 \end{bmatrix}, \tag{1}$$

where the row and column indices correspond to the current and next state, respectively. The maximum entropy achieving transition probability matrix $\mathbf{P} \in \mathbb{R}^{(d+1)\times(d+1)}$ can be obtained as [35, eq. (2.23)]

$$[\mathbf{P}]_{i,j} = \frac{b_j}{b_i} \frac{[\mathbf{A}_d]_{i,j}}{\lambda_{\max}}, \tag{2}$$

where $\lambda_{\max}$ corresponds to the largest eigenvalue such that $\mathbf{A}_d\mathbf{b} = \lambda_{\max}\mathbf{b}$ and b_i denotes the ith element of $\mathbf{b}$. In the remainder of this work, we refer to RLL sequences following the state transition probabilities given in (2) as *maximum entropy* RLL sequences. Their capacity in bit per symbol is given by $C(d, k) = \log_2(\lambda_{\max})$ [35, eq. (2.19)], for which some numerical values are given in Table 1. The reader is referred to [19], [35] for more information on RLL sequences.

TABLE 1. Maximum achievable rate of ZXM.

Constraint (d, k)	$(0, \infty)$	$(1, \infty)$	$(2, \infty)$	$(3, \infty)$	$(4, \infty)$
Capacity $C(d, k)$ [bit/symbol]	1	0.694	0.551	0.465	0.406
FTN factor M_{Tx}	1	2	3	4	5
Rate $R_{\max}^{\mathrm{ZXM}}$ [bit/T_{N}/dim]	1	1.388	1.653	1.860	2.030

C. ZERO-CROSSING MODULATION

As mentioned above, we implement ZXM by combining M_{Tx}-fold FTN signaling with RLL transmit sequences, i.e., transmitting M_{Tx} RLL symbols per Nyquist interval. Here, we always choose the d constraint as $d = M_{\mathrm{Tx}} - 1$, which ensures that the same amplitude is kept for at least one Nyquist interval. This choice results in a maximum rate of $R_{\max}^{\mathrm{ZXM}} = M_{\mathrm{Tx}}\, C(d, k)$ bit per Nyquist interval per real signaling dimension. Some numerical values of $R_{\max}^{\mathrm{ZXM}}$ are provided in Table 1, where the column '$(0, \infty)$' corresponds to standard BPSK. It can be observed that the rate loss due to the RLL constraint is overcompensated by simultaneously employing FTN signaling. Moreover, note that even larger transmission rates can be obtained by further increasing M_{Tx} and d.

III. SYSTEM MODEL

In this section, we introduce the system model, which is illustrated in Fig. 2. The transmit signal, channel model and analog combiner, and the received signal are detailed in Sections III-A–III-C, respectively. Finally, an equivalent discrete-time system model, which is used to derive the equalizer in Section IV-B, is introduced in Section III-D. This work focuses on the receiver design. Hence, transmit beamforming is omitted. We employ root-raised-cosine (RRC) transmit and receive filters, denoted by $f(t)$ and $g(t)$, respectively. Furthermore, we assume perfect synchronization[1] and channel parameter information at the receiver throughout this work.

A. TRANSMIT SIGNAL

The transmitter employs ZXM, which is implemented by combining FTN signaling and RLL transmit sequences (cf. Section II). The input at the transmitter is given by a sequence of payload bits i_ℓ. After forward error correction (FEC) encoding, interleaving and RLL encoding, the complex-valued sequence of $m \in \mathbb{N}$ transmit symbols, denoted as $\mathbf{x}^m$, is constructed from two independently modulated RLL sequences $\mathbf{a}^m, \mathbf{b}^m \in \{+1, -1\}^m$, such that

$$\mathbf{x}^m = \frac{1}{\sqrt{2}}\left(\mathbf{a}^m + j\mathbf{b}^m\right), \tag{3}$$

i.e., we employ ZXM on the in-phase and quadrature component. Note that we present a method of encoding bits onto

1. Synchronization for systems employing 1-bit quantization and temporal oversampling is an ongoing research topic; bounds are studied in [36].

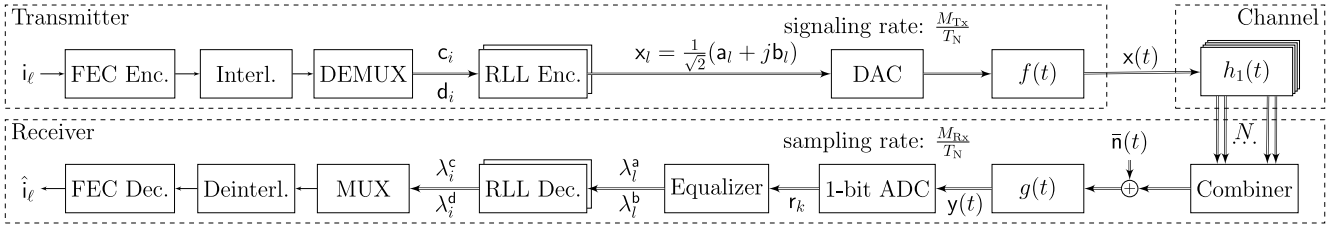

FIGURE 2. Overview of the system model, where i_ℓ corresponds to the input bits to be transmitted and $\hat{\mathsf{i}}_\ell$ to their estimates at the receiver.

RLL sequences in Section IV-A. Then, the continuous-time transmit signal is given by

$$\mathsf{x}(t) = \sum_{l=1}^{m} \mathsf{x}_l f\left(t - \frac{lT_{\mathrm{N}}}{M_{\mathrm{Tx}}}\right), \tag{4}$$

where $M_{\mathrm{Tx}} \in [1, \infty)$ denotes the FTN signaling factor, T_{N} denotes the Nyquist interval, which is defined by the RRC transmit filter $f(t)$, and x_l denotes the lth element of $\mathbf{x}^m$.

B. CHANNEL AND ANALOG COMBINING

In this work, we consider a single user uplink scenario, where the transmitter and receiver are equipped with a single antenna and a uniform rectangular array (URA), respectively. The URA at the receiver consists of $N = N_{\mathrm{h}} \cdot N_{\mathrm{v}}$ antennas, where the number of horizontal and vertical antennas are written as N_{h} and N_{v}, respectively.

After beam alignment, the effective channel typically consists only of a single dominant path [33]. Hence, we consider a LOS channel which is characterized by the angles-of-arrival (AoAs), i.e., the azimuth angle $\phi \in [-\pi, \pi)$ and the elevation angle $\theta \in [-\frac{\pi}{2}, \frac{\pi}{2})$. When the receiver is located in the far-field of the transmitter, the propagation delay between the nth receive antenna and the center of the URA can be defined as (cf. [37, Sec. 2.2])

$$\tau_n = \frac{1}{c}\mathbf{k}(\phi, \theta)^T(\mathbf{u}_n - \bar{\mathbf{u}}), \quad n \in \mathcal{N} = \{1, \ldots, N\}, \tag{5}$$

where c denotes the speed of light and $\mathbf{k}(\phi, \theta)$ denotes the wave vector normalized to unit length, which is given by

$$\mathbf{k}(\phi, \theta) = \begin{bmatrix} -\cos\theta\cos\phi \\ -\cos\theta\sin\phi \\ -\sin\theta \end{bmatrix}. \tag{6}$$

Moreover, $\mathbf{u}_n \in \mathbb{R}^3$ and $\bar{\mathbf{u}} \in \mathbb{R}^3$ denote the position of the nth receive antenna and the center of the URA, respectively, which are defined as

$$\mathbf{u}_n = \begin{bmatrix} 0 \\ \mathrm{mod}(n-1, N_{\mathrm{h}})\, d_{\mathrm{h}} \\ \lfloor (n-1)/N_{\mathrm{h}} \rfloor\, d_{\mathrm{v}} \end{bmatrix}, \quad \bar{\mathbf{u}} = \begin{bmatrix} 0 \\ \frac{(N_{\mathrm{h}}-1)d_{\mathrm{h}}}{2} \\ \frac{(N_{\mathrm{v}}-1)d_{\mathrm{v}}}{2} \end{bmatrix}, \tag{7}$$

where d_{h} and d_{v} correspond to the horizontal and vertical antenna spacing, respectively. The complex baseband channel impulse response from the transmitter to the nth receive antenna is then given by

$$h_n(t) = \frac{1}{\sqrt{N}}\delta(t - \tau_n)e^{-j2\pi f_{\mathrm{c}}\tau_n}, \quad n \in \mathcal{N} \tag{8}$$

where f_{c} denotes the carrier frequency. Note that the sum of all channels is normalized to unit energy, i.e., there is no path loss.

Observing (8), it can be seen that the physical propagation delay, given by (5), results in a time- and a phase-shift in the channel model. Hence, due to the time-shift, the received signal at different antennas can correspond to different transmit symbols. This effect is known as SWE [32]. In narrowband systems, this time-shift may be neglected, i.e., the channel can be approximated as $h_n(t) \approx \frac{1}{\sqrt{N}}e^{-j2\pi f_{\mathrm{c}}\tau_n}$ [37, Sec. 2.2]. However, this assumption is expected to be invalid here, as we target wideband channels.

The receiver employs analog combining, which is implemented using a PSN, i.e., a digitally controllable phase-shift is applied to the received signal of each antenna before the signals of all antennas are superimposed in the analog domain. This analog combining architecture is considered to be well suited for low-cost systems. We model the phase shifters as *pure* phase shifters, i.e., they do not introduce any additional time delay.[2] The phase-shift induced by the nth phase shifter is represented by $\frac{1}{\sqrt{N}}e^{j\psi_n}$, $n \in \mathcal{N}$. In order to compensate the phase-shift introduced by the channel, the optimal phase-shift at the nth antenna is

$$\psi_n^{\mathrm{opt}} = 2\pi f_{\mathrm{c}}\tau_n. \tag{9}$$

Note that implementing (9) requires infinite resolution phase shifters and that the PSN cannot compensate for the time delays introduced by the channel (cf. (8)). Consequently, combining the signals obtained at the different antennas in the analog PSN generally introduces additional ISI due to *incoherent* superposition. This effect is illustrated in Fig. 3.

C. RECEIVED SIGNAL

The received signal at the nth antenna is described by combining the transmit signal given in (4) with the channel model given in (8), which yields

$$\begin{aligned}\tilde{\mathsf{y}}_n(t) &= (\mathsf{x} * h_n)(t) + \tilde{\mathsf{n}}_n(t) \\ &= \frac{1}{\sqrt{N}}\sum_{l=1}^{m} \mathsf{x}_l f\left(t - \frac{lT_{\mathrm{N}}}{M_{\mathrm{Tx}}} - \tau_n\right)e^{-j2\pi f_{\mathrm{c}}\tau_n} + \tilde{\mathsf{n}}_n(t),\end{aligned} \tag{10}$$

2. This model is valid, e. g., for reflection-type or vector-modulator implementations.

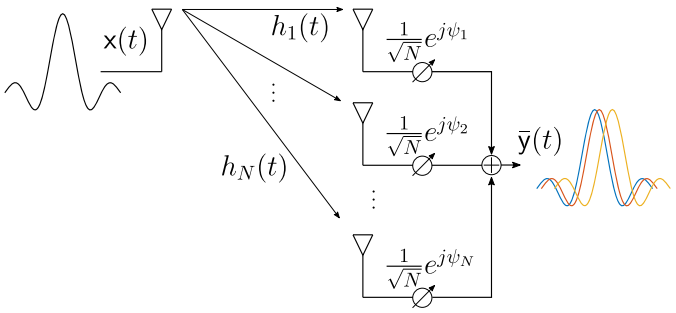

FIGURE 3. Because the analog PSN cannot compensate any delays, the wideband received signals may be combined *incoherently*.

where $\tilde{n}_n(t)$ denotes the complex AWGN process at the nth antenna. After analog combining and filtering by $g(t)$, the received signal at the input of the 1-bit ADC is given by

$$\begin{aligned} y(t) &= \left(\frac{1}{\sqrt{N}}\sum_{n=1}^{N}\tilde{y}_n(t)\,e^{j\psi_n}\right) * g(t) \\ &= \sum_{l=1}^{m} x_l\,\bar{v}\left(t - \frac{lT_N}{M_{Tx}}\right) + \big(\bar{n} * g\big)(t), \end{aligned} \tag{11}$$

with

$$\bar{n}(t) = \frac{1}{\sqrt{N}}\sum_{n=1}^{N}\tilde{n}_n(t)\,e^{j\psi_n}, \tag{12}$$

$$\bar{v}(t) = \frac{1}{N}\sum_{n=1}^{N} v(t-\tau_n)e^{j(\psi_n - 2\pi f_c\tau_n)}, \tag{13}$$

where the combined transmit and receive filter is written as $v(t) = (f * g)(t)$. Furthermore, $\bar{v}(t)$, given in (13), models the combined effects of transmit filtering, receive filtering, and incoherent analog combining. Note that we also normalize the analog combiner by $\frac{1}{\sqrt{N}}$ to ensure an overall unit energy normalization, i.e., the considered system model does not contain any path loss nor any beamforming gain.

Sampling the received signal $y(t)$ with rate $\frac{M_{Rx}}{T_N}$, where M_{Rx} denotes the temporal oversampling factor w. r. t. the Nyquist rate, yields for the kth sample

$$y_k = \sum_{l=1}^{m} x_l\,\bar{v}\left(\frac{kT_N}{M_{Rx}} - \frac{lT_N}{M_{Tx}}\right) + \big(\bar{n} * g\big)\left(\frac{kT_N}{M_{Rx}}\right). \tag{14}$$

Subsequently, the real and imaginary part of the received signal are independently 1-bit quantized, which yields

$$r_k = \mathcal{Q}_1(y_k) = p_k + jq_k, \tag{15}$$

with $p_k = \operatorname{sign}(\Re\{y_k\})$ and $q_k = \operatorname{sign}(\Im\{y_k\})$, where we define the signum function as $\operatorname{sign}(x') = 1$ if $x' \geq 0$ and $\operatorname{sign}(x') = -1$ if $x' < 0$.

D. EQUIVALENT DISCRETE-TIME SYSTEM MODEL

In this section, we detail an equivalent matrix-vector notation of the system model derived in Sections III-A and III-C, as well as an auxiliary channel. This discrete-time model is used in Section IV-B to derive the equalizer. Following a similar approach as in [16], [17], we introduce an effective oversampling factor $M = \frac{M_{Rx}}{M_{Tx}}$. Note that $M = 1$ corresponds to sampling at signaling rate, while $M > 1$ denotes oversampling w. r. t. the signaling rate $\frac{M_{Tx}}{T_N}$. For *integer* effective oversampling factors, i.e., $M \in \mathbb{N}$, an equivalent discrete-time system model is given by

$$\mathbf{r}_{l'} = \mathcal{Q}_1\Big(\bar{\mathbf{V}}_\infty \mathbf{U}_\infty \mathbf{x}^{l'}_{l'-L_\infty} + \mathbf{n}^{\text{ch}}_{l'}\Big), \tag{16}$$

where l' denotes the transmit symbol index and we use the notation $\mathbf{x}^{l'}_{l'-L_\infty} = [x_{l'-L_\infty}, \ldots, x_{l'}]^T$. The vector $\mathbf{r}_{l'} \in \mathbb{C}^M$ contains M complex 1-bit quantized samples which we associate with the transmit symbol $x_{l'}$, but which also depend on the $L_\infty \in \mathbb{N}$ previous transmit symbols. Consequently, we refer to L_∞ as memory length of the ISI channel, measured in transmit symbols. Note that L_∞ is in general infinite for the considered RRC transmit and receive filters. Therefore, in practice, L_∞ is truncated to a large but finite length. The matrix $\bar{\mathbf{V}}_\infty \in \mathbb{C}^{M\times M(L_\infty+1)}$ is a Toeplitz matrix which contains the effective filter (13); it is given by

$$\bar{\mathbf{V}}_\infty = \begin{bmatrix} \big[\ \bar{\mathbf{v}}_r^T\ \big] & 0\cdots & 0 \\ 0 & \big[\ \bar{\mathbf{v}}_r^T\ \big] & 0\cdots 0 \\ & \ddots & \ddots & \ddots \\ 0\cdots & 0 & \big[\ \bar{\mathbf{v}}_r^T\ \big] \end{bmatrix}, \tag{17}$$

with

$$\begin{aligned} \bar{\mathbf{v}}_r^T = \Bigg[&\bar{v}\left(\frac{K_\infty}{2}\frac{T_N}{M_{Rx}}\right), \ldots, \bar{v}\left(\frac{T_N}{M_{Rx}}\right), \bar{v}\left(0\right), \\ &\bar{v}\left(-\frac{T_N}{M_{Rx}}\right), \ldots, \bar{v}\left(-\frac{K_\infty}{2}\frac{T_N}{M_{Rx}}\right)\Bigg], \end{aligned} \tag{18}$$

where $K_\infty = L_\infty M$ denotes the ISI memory length measured in samples at the receiver, which is assumed to be even, i.e., corresponding to symmetric filters. Moreover, we introduce an upsampling matrix, denoted as $\mathbf{U}_\infty \in \mathbb{R}^{M(L_\infty+1)\times L_\infty+1}$, which inserts $M-1$ zeros after each element of $\mathbf{x}^{l'}_{l'-L_\infty}$. It is given by

$$[\mathbf{U}_\infty]_{i,j} = \begin{cases} 1, & \text{for } i = 1 + (j-1)\cdot M \\ 0, & \text{else,} \end{cases} \tag{19}$$

with $i \in \{1, \ldots, M(L_\infty+1)\}$, $j \in \{1, \ldots, L_\infty+1\}$. Note that upsampling of the transmit symbol sequence is necessary to match the signaling and sampling rate for $M > 1$. The AWGN noise process at the receiver is denoted by $\mathbf{n}^{\text{ch}}_{l'}$, which is correlated for $M_{Rx} > 1$ because of receive filtering and temporal oversampling. For the considered RRC receive filter, the covariance matrix $\mathbf{\Sigma}^{\text{ch}}_{\mathbf{n}}$ of $\mathbf{n}^{\text{ch}}_{l'}$ is given by (cf. [38, eq. (9-2-27)])

$$\left[\mathbf{\Sigma}^{\text{ch}}_{\mathbf{n}}\right]_{i,j} = \sigma_n^2 \frac{\sin(\pi|i-j|/M_{Rx})}{\pi|i-j|/M_{Rx}} \frac{\cos(\pi\beta|i-j|/M_{Rx})}{1-(2\beta|i-j|/M_{Rx})^2}, \tag{20}$$

where $\sigma_n^2 = \frac{N_0}{T_N}$ and β denote the noise variance and the roll-off factor, respectively. Finally, stacking all received vectors yields $\mathbf{r}^{\bar{m}} = [\mathbf{r}_1^T, \ldots, \mathbf{r}_m^T]^T$, with $\bar{m} = mM$.

1) AUXILIARY CHANNEL

To facilitate equalization of the 1-bit quantized ISI channel given in (16), our goal is to obtain an approximate system model with a reduced memory length $L < L_\infty$, where $L \in \mathbb{N}$ is assumed to be even, i.e., corresponding to symmetric filters. To this aim, we introduce the following block matrix

$$\left[\bar{\mathbf{W}}_L, \bar{\mathbf{W}}, \bar{\mathbf{W}}_R\right] = \bar{\mathbf{V}}_\infty \mathbf{U}_\infty, \tag{21}$$

where $\bar{\mathbf{W}}_L \in \mathbb{C}^{M\times\tilde{L}}$, $\bar{\mathbf{W}} \in \mathbb{C}^{M\times(L+1)}$ and $\bar{\mathbf{W}}_R \in \mathbb{C}^{M\times\tilde{L}}$ with $\tilde{L} = \frac{L_\infty - L}{2}$. Note that for the considered RRC transmit and receive filters, the dominant ISI components are contained in $\bar{\mathbf{W}}$. We obtain the following approximation of (16), by approximating the ISI components not contained in $\bar{\mathbf{W}}$ by an additional complex-valued Gaussian noise process,

$$\mathbf{r}_l \approx \mathcal{Q}_1\Big(\bar{\mathbf{W}}\mathbf{x}_{l-L}^{l} + \mathbf{n}_l^{\mathrm{ISI}} + \mathbf{n}_l^{\mathrm{ch}}\Big), \tag{22}$$

with $l = l' - \tilde{L}$ and $\mathbf{n}_l^{\mathrm{ISI}} \sim \mathcal{CN}(\mathbf{0}_M, \mathbf{\Sigma}_{\mathbf{n}}^{\mathrm{ISI}})$. The covariance matrix $\mathbf{\Sigma}_{\mathbf{n}}^{\mathrm{ISI}}$ is therein approximated as $\mathbf{\Sigma}_{\mathbf{n}}^{\mathrm{ISI}} \approx \bar{\mathbf{W}}_L \mathbf{\Sigma}_{\mathbf{x}} \bar{\mathbf{W}}_L^H + \bar{\mathbf{W}}_R \mathbf{\Sigma}_{\mathbf{x}} \bar{\mathbf{W}}_R^H$, with $\mathbf{\Sigma}_{\mathbf{x}} \in \mathbb{R}^{\tilde{L}\times\tilde{L}}$,

$$[\mathbf{\Sigma}_{\mathbf{x}}]_{i,j} = R_{\mathsf{x}}[i-j], \tag{23}$$

where $R_{\mathsf{x}}[n]$ denotes the autocorrelation of the RLL sequence, which is given in (51). The approximation is due to ignoring the cross-terms, which are assumed to be negligible because the autocorrelation decays quickly. Note that in contrast to the auxiliary channel from [20], the presented auxiliary channel takes into account the correlation in the ISI noise components.

2) EQUIVALENT REAL-VALUED DISCRETE-TIME SYSTEM MODEL

For equalization, it is useful to convert the complex-valued approximate system model from (22) to an equivalent real-valued system model. Therefore, we first combine the noise components, i.e., $\mathbf{n}_l = \mathbf{n}_l^{\mathrm{ISI}} + \mathbf{n}_l^{\mathrm{ch}}$, such that $\mathbf{n}_l \sim \mathcal{CN}(\mathbf{0}_M, \mathbf{\Sigma}_{\mathbf{n}})$ with

$$\mathbf{\Sigma}_{\mathbf{n}} = \mathbf{\Sigma}_{\mathbf{n}}^{\mathrm{ISI}} + \mathbf{\Sigma}_{\mathbf{n}}^{\mathrm{ch}}. \tag{24}$$

Then, an equivalent real-valued version of (22) is obtained as

$$\begin{bmatrix}\Re\{\mathbf{r}_l\}\\ \Im\{\mathbf{r}_l\}\end{bmatrix} = \begin{bmatrix}\mathbf{p}_l\\ \mathbf{q}_l\end{bmatrix} \approx \mathrm{sign}\left(\begin{bmatrix}\mathbf{z}_l^{\mathrm{R}}\\ \mathbf{z}_l^{\mathrm{I}}\end{bmatrix}\right), \tag{25}$$

where the signum function is employed element-wise and

$$\begin{bmatrix}\mathbf{z}_l^{\mathrm{R}}\\ \mathbf{z}_l^{\mathrm{I}}\end{bmatrix} = \frac{1}{\sqrt{2}}\begin{bmatrix}\Re\{\bar{\mathbf{W}}\} & -\Im\{\bar{\mathbf{W}}\}\\ \Im\{\bar{\mathbf{W}}\} & \Re\{\bar{\mathbf{W}}\}\end{bmatrix}\begin{bmatrix}\mathbf{a}_{l-L}^{l}\\ \mathbf{b}_{l-L}^{l}\end{bmatrix} + \begin{bmatrix}\Re\{\mathbf{n}_l\}\\ \Im\{\mathbf{n}_l\}\end{bmatrix}. \tag{26}$$

IV. PROPOSED TRANSCEIVER DESIGN

In this section, we detail the proposed transceiver design. First, we describe encoding of bits onto RLL sequences by deriving four FSM RLL encoders[3] in Section IV-A. Then, we present the soft-output equalizer and the SISO RLL decoder in Section IV-B and Section IV-C, respectively. Finally, an overall discussion of the proposed transceiver design is provided in Section IV-D. Note that the transceiver additionally consists of a FEC encoder and decoder, which are, however, not studied in this work.

3. MATLAB functions implementing the presented RLL encoding and SISO RLL decoding are available under: https://github.com/vodafone-chair/rll-lib.

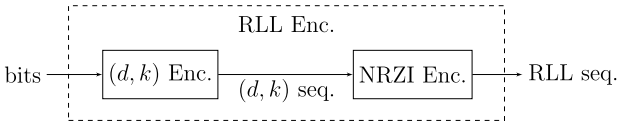

FIGURE 4. Considered RLL encoder architecture.

TABLE 2. Comparison of derived finite-state machine RLL codes.

RLL const. (d,k)	Capacity $C(d,k)$ [bit/symbol]	FSM code rate R_{RLL} [bit/symbol]	Efficiency η
$(1,\infty)$	0.694	2/3	96.1 %
$(2,\infty)$	0.551	1/2	90.7 %
$(3,\infty)$	0.465	3/7	92.2 %
$(4,\infty)$	0.406	3/8	92.4 %

A. RLL ENCODING

In this subsection, we introduce a practical RLL encoding scheme, i.e., a mapping of bits onto RLL sequences. We focus on *fixed-length* FSM RLL codes throughout this work. Alternative encoding schemes are discussed in Section IV-D. As described in Section II-B, RLL encoding is typically divided into two steps (cf. Fig. 4): *i*) encoding of bits onto (d,k) sequences, and *ii*) converting the (d,k) sequence into an RLL sequence by NRZI encoding. In the following, we focus on encoding of bits onto (d,k) sequences, as the subsequent NRZI encoding step is trivial.

The code rate of any practical RLL encoder, denoted as R_{RLL}, is upper-bounded by the capacity $C(d,k)$ of the corresponding maximum entropy RLL sequences, i.e., $R_{\mathrm{RLL}} \leq C(d,k)$. Some numerical values of $C(d,k)$ are given in Table 1. The ratio $\eta = \frac{R_{\mathrm{RLL}}}{C(d,k)}$ measures how close the code rate of an encoder is to the capacity $C(d,k)$, i.e., it measures the encoder efficiency. It is intuitive to seek encoders which closely approximate the properties of maximum entropy RLL sequences, i.e., encoders with a high efficiency η.

FSM (d,k) codes can be derived from the FSM description of the (d,k) constraint (cf. Fig. 1) using an algorithm which is known as Adler-Coppersmith-Hassner (ACH) [39] or state-splitting algorithm [40, Ch. 5]. For any $p,q \in \mathbb{N}$, such that $R_{\mathrm{RLL}} = \frac{p}{q} \leq C(d,k)$, the algorithm can be used to derive FSM (d,k) codes with rate R_{RLL}, i.e., blocks of p input bits are mapped onto (d,k) sequence segments of length q.

In this work, we derive four FSM $(d, k=\infty)$ encoders for $d = \{1,2,3,4\}$ using the ACH algorithm. The tables defining the resulting encoders are delegated to Appendix A, i.e., they are defined by Tables 3 to 6. Table 2 provides a comparison of the encoder parameters. It can be seen that the coding efficiency of all derived FSM (d,k) codes is above 90 %.

B. SOFT-OUTPUT EQUALIZER

This subsection introduces the equalizer, which corresponds to the first digital signal processing block at the receiver (cf. Fig. 2). The MAP RLL symbol detection problem can be formulated as

$$\hat{x}_l = \underset{x_l \in \mathcal{X}}{\operatorname{argmax}} P\left(x_l \middle| \mathbf{r}^{\bar{m}}\right), \quad \forall l \in \{1, \ldots, m\}, \tag{27}$$

where $\mathbf{r}^{\bar{m}}$ denotes a realization of the 1-bit quantized observation vector. To enable an efficient implementation, it is required to obtain a factorization of the a posteriori probability (APP) $P(\mathbf{x}^m|\mathbf{r}^{\bar{m}})$. From Bayes' theorem it follows

$$P\left(\mathbf{x}^m \middle| \mathbf{r}^{\bar{m}}\right) = \frac{P\left(\mathbf{r}^{\bar{m}} \middle| \mathbf{x}^m\right) P(\mathbf{x}^m)}{P\left(\mathbf{r}^{\bar{m}}\right)}. \tag{28}$$

Therein, the a priori probability $P(\mathbf{x}^m)$ can be factorized as

$$P\left(\mathbf{x}^m\right) = P\left(\mathbf{a}^m\right) P\left(\mathbf{b}^m\right) = \prod_{l=1}^{m} P\left(a_l \middle| \mathbf{a}^{l-1}\right) P\left(b_l \middle| \mathbf{b}^{l-1}\right), \tag{29}$$

where $P(a_l|\mathbf{a}^{l-1})$ and $P(b_l|\mathbf{b}^{l-1})$ correspond to the state transition probability of the underlying RLL sequence, which is given in (2) for maximum entropy RLL sequences.

Factorizing $P(\mathbf{r}^{\bar{m}}|\mathbf{x}^m)$ is generally not possible due to the noise correlation. Hence, we obtain an *approximate* factorization by neglecting the noise correlation between received signal vectors corresponding to different transmit symbols, e.g., between $\mathbf{r}_l$ and $\mathbf{r}_{l+1}$ (cf. (16)). Then, $P(\mathbf{r}^{\bar{m}}|\mathbf{x}^m)$ can be factorized as

$$P\left(\mathbf{r}^{\bar{m}} \middle| \mathbf{x}^m\right) = P\left(\mathbf{p}^{\bar{m}} \middle| \mathbf{x}^m\right) P\left(\mathbf{q}^{\bar{m}} \middle| \mathbf{x}^m\right) \tag{30}$$

$$\approx \prod_{l=1}^{m} P\left(\mathbf{p}_l \middle| \mathbf{x}^l\right) P\left(\mathbf{q}_l \middle| \mathbf{x}^l\right), \tag{31}$$

where

$$P\left(\mathbf{p}_l | \mathbf{x}^l\right) = \int_{\mathcal{P}_l^{\mathcal{M}}} P\left(\mathbf{z}_l^{\mathrm{R}} | \mathbf{x}^l\right) \mathrm{d}\, \mathbf{z}_l^{\mathrm{R}}. \tag{32}$$

Therein, $\mathbf{z}_l^{\mathrm{R}}$ denotes the real part of the quantizer input given in (25). The integration region $\mathcal{P}_l^{\mathcal{M}} = \mathcal{P}_{l,1} \times \ldots \times \mathcal{P}_{l,M}$ is defined by the real part of the 1-bit quantizer output, i.e., the first component of the left-hand side (LHS) of (25), according to

$$\mathcal{P}_{l,m} = \begin{cases} (-\infty, 0), & \text{for } p_{l,m} = -1 \\ [0, \infty), & \text{for } p_{l,m} = +1, \end{cases}, \quad m \in \{1, \ldots, M\}, \tag{33}$$

and the probability density function (PDF) $P(\mathbf{z}_l^{\mathrm{R}}|\mathbf{x}^l)$ is given by

$$P\left(\mathbf{z}_l^{\mathrm{R}} \middle| \mathbf{x}^l\right) = \frac{1}{\sqrt{(2\pi)^M |\tilde{\mathbf{\Sigma}}_{\mathbf{n}}|}} e^{-\frac{1}{2}\left(\mathbf{z}_l^{\mathrm{R}} - \boldsymbol{\mu}_{\mathrm{R}}(\mathbf{x}^l)\right)^T \tilde{\mathbf{\Sigma}}_{\mathbf{n}}^{-1} \left(\mathbf{z}_l^{\mathrm{R}} - \boldsymbol{\mu}_{\mathrm{R}}(\mathbf{x}^l)\right)} \tag{34}$$

with mean

$$\boldsymbol{\mu}_{\mathrm{R}}\left(\mathbf{x}^l\right) = \frac{1}{\sqrt{2}} \begin{bmatrix} \Re\{\bar{\mathbf{W}}\} & -\Im\{\bar{\mathbf{W}}\} \end{bmatrix} \begin{bmatrix} \mathbf{a}_{l-L}^{l} \\ \mathbf{b}_{l-L}^{l} \end{bmatrix}, \tag{35}$$

and covariance $\tilde{\mathbf{\Sigma}}_{\mathbf{n}} = \frac{1}{2}\mathbf{\Sigma}_{\mathbf{n}}$, which is defined in (24). $P(\mathbf{q}_l|\mathbf{x}^l)$ is defined similar to $P(\mathbf{p}_l|\mathbf{x}^l)$. Inserting (29) and (31) into (28) yields the APP factorization

$$P\left(\mathbf{x}^m \middle| \mathbf{r}^{\bar{m}}\right) \approx \frac{\prod_{l=1}^{m} P\left(\mathbf{p}_l|\mathbf{x}^l\right) P\left(\mathbf{q}_l|\mathbf{x}^l\right) P\left(a_l|\mathbf{a}^{l-1}\right) P\left(b_l|\mathbf{b}^{l-1}\right)}{P\left(\mathbf{r}^{\bar{m}}\right)}. \tag{36}$$

1) BCJR ALGORITHM

The Bahl-Cocke-Jelinek-Raviv (BCJR) algorithm [41] allows for an efficient implementation of MAP symbol detection. The algorithm works on a trellis, where each trellis state $s_l \in \mathcal{S}$ at time instance l is associated with the previous real and imaginary inputs of memory length L, such that

$$s_{l-1} \stackrel{\wedge}{=} \begin{bmatrix} \mathbf{a}_{l-L}^{l-1} \\ \mathbf{b}_{l-L}^{l-1} \end{bmatrix}. \tag{37}$$

In (37), the LHS is a shorthand notation for the vector on the right-hand side (RHS), which corresponds to a certain realization of transmitted RLL sequences. To emphasize this, we use the notation '$\stackrel{\wedge}{=}$'. The state transition probability $\gamma_l(s_{l-1}, s_l)$ between two states $s_{l-1}, s_l \in \mathcal{S}$ at time instance l depends on the observation $\mathbf{r}_l$ and is defined as

$$\gamma_l(s_{l-1}, s_l) = P(\mathbf{r}_l|s_{l-1}, s_l) P(s_l|s_{l-1}) \tag{38}$$

$$\approx P\left(\mathbf{p}_l \middle| \mathbf{x}^l\right) P\left(\mathbf{q}_l \middle| \mathbf{x}^l\right) P\left(a_l \middle| \mathbf{a}^{l-1}\right) P\left(b_k \middle| \mathbf{b}^{l-1}\right), \tag{39}$$

where (39) is due to (31). The BCJR algorithm recursively iterates through the trellis. Using (38), the corresponding forward and backward recursions can be obtained as

$$\alpha(s_l) = \sum_{s_{l-1} \in \mathcal{S}} \alpha(s_{l-1}) \gamma_l(s_{l-1}, s_l) \tag{40}$$

and

$$\beta(s_l) = \sum_{s_{l+1} \in \mathcal{S}} \beta(s_{l+1}) \gamma_{l+1}(s_l, s_{l+1}), \tag{41}$$

respectively. In practice, the recursions have to be initialized appropriately, e. g., by starting and terminating in known states. Moreover, it is common practice to implement a normalization step in each recursion for numerical stability [42]. Then, by combining (38), (40) and (41), the joint probability $P(s_{l-1}, s_l, \mathbf{r}^{\bar{m}})$ can be factorized as

$$P\left(s_{l-1}, s_l, \mathbf{r}^{\bar{m}}\right) = \alpha(s_{l-1}) \gamma_l(s_{l-1}, s_l) \beta(s_l). \tag{42}$$

The joint probability in (42) can be utilized to compute LLRs. To this end, we denote the sets of state transition tuples (s_{l-1}, s_l) which result in a transmit symbol at time

instance l of $\mathsf{a}_l = +1$ and $\mathsf{a}_l = -1$ as $\mathcal{T}_{\mathsf{a}}^{+}$ and $\mathcal{T}_{\mathsf{a}}^{-}$, respectively. Then, the corresponding LLRs are defined as

$$\lambda_l^{\mathsf{a}} = \log \frac{\sum_{(s,s')\in\mathcal{T}_{\mathsf{a}}^{+}} P\left(s_{l-1}=s, s_l=s', \mathbf{r}^{\tilde{m}}\right)}{\sum_{(s,s')\in\mathcal{T}_{\mathsf{a}}^{-}} P\left(s_{l-1}=s, s_l=s', \mathbf{r}^{\tilde{m}}\right)}, \tag{43}$$

for all $l \in \{1,\ldots,m\}$. Note that (43) provides soft-information for each RLL symbol of the real part, i.e., of $\mathbf{a}^m$. LLRs for the RLL symbols of the imaginary part, denoted as λ_l^{b}, can be obtained similarly. Both resulting LLR sequences can be processed independently afterwards. The equalizer proposed here bears some similarity to the *quantized BCJR* proposed in [28]. However, the proposed equalizer utilizes the RLL constraint to reduce the number of trellis states and transitions, makes use of the a priori knowledge of the RLL transition probabilities, and also supports temporal oversampling.

2) COMPLEXITY

The implementation complexity of the BCJR equalizer mainly depends on the number of trellis states $|\mathcal{S}|$, which in turn depends on the number of valid RLL sequences of length L (cf. (37)). We note that the number of $(d, k=\infty)$ sequences of length L is given by the following recursion [35, Sec. 4.2]

$$\tilde{\zeta}_d(L) = \begin{cases} L+1, & 1 \le L \le d+1 \\ \tilde{\zeta}_d(L-1) + \tilde{\zeta}_d(L-d-1), & L > d+1, \end{cases} \tag{44}$$

where the first case is due to the fact that for $L \le d+1$, the sequence either only contains '0's or a single '1'. When converting the $(d, k=\infty)$ sequences into RLL sequences by NRZI encoding, the number of sequences generally doubles, as one can start either with '+1' or '−1'. However, the all zero (d,k) sequence and the (d,k) sequence which starts with a '1' are mapped onto the same RLL sequences. Hence, the number of RLL sequences of length L can be obtained by the following modified recursion

$$\zeta_d(L) = \begin{cases} 2L, & 1 \le L \le d+1 \\ \zeta_d(L-1) + \zeta_d(L-d-1), & L > d+1. \end{cases} \tag{45}$$

Thus, the number of trellis states is given by $|\mathcal{S}| = \zeta_d^2(L)$, as it corresponds to all possible combinations of two RLL sequences of length L (cf. (37)).

It can be verified that the number of trellis state transitions is given by $|\mathcal{T}| = \zeta_d^2(L+1)$, because each RLL sequence of length $L+1$ has a unique predecessor RLL sequence of length L. The main computational complexity in the equalizer stems from evaluating the state transition probabilities $\gamma_l(s_{l-1}, s_l)$, which involves numerical integration. However, for the considered system model, they can be obtained offline under the assumption that the phase-shifts are perfectly compensated, i.e., $\psi_n = \psi_n^{\text{opt}}$ (cf. Section III-B). Alternatively, the M-dimensional numerical integration in (32) might be approximated by M Q-function evaluations, which can, e. g., be implemented using look-up tables. Note that this approximation corresponds to ignoring the noise correlation in $\mathbf{n}_l$.

In the following, we evaluate the complexity in terms of the number of additions and multiplications. For simplicity we count divisions as multiplications. As the equalizer performs joint equalization of the RLL symbols in the real and imaginary part of the transmit signal, we normalize the number of operations to the number of RLL symbols x_l, i.e., we count the number of operations to produce an LLR tuple $(\lambda_l^{\mathsf{a}}, \lambda_l^{\mathsf{b}})$.

Under the assumption that $\gamma_l(s_{l-1}, s_l)$ is known, the number of additions per LLR tuple at the equalizer output is given by $N_{\text{add}} = 4|\mathcal{T}|$: The forward and backward recursions each require $|\mathcal{T}|$ additions per time instance l. Evaluating (43) twice, i.e., once for λ_l^{a} and once for λ_l^{b}, requires an additional $2|\mathcal{T}|$ additions, because it holds $|\mathcal{T}_{\mathsf{a}}^{+}| + |\mathcal{T}_{\mathsf{a}}^{-}| = |\mathcal{T}|$. Similarly, the number of multiplications per LLR tuple at the equalizer output is given by $N_{\text{mult}} = 4|\mathcal{T}| + 2$: The forward and backward recursions require $|\mathcal{T}|$ multiplications each. Evaluating (42) for all transitions requires $2|\mathcal{T}|$ multiplications. Finally, evaluating (43) twice, i.e., once for λ_l^{a} and once for λ_l^{b}, requires 2 additional divisions.

C. SOFT-INPUT SOFT-OUPUT RLL DECODER

Soft-input soft-output joint NRZI and (d,k) decoding of the FSM RLL codes can be implemented again using the BCJR algorithm [41]. Implementing *joint* NRZI and (d,k) decoding has the advantage that it omits implementing additional SISO NRZI decoding. Note that the decoding procedure is similar to SISO decoding of convolutional codes (cf. [42, Sec. II.C]). To ease the explanation, we show how to convert the LLRs per RLL symbol $\{\lambda_l^{\mathsf{a}}\}$ to LLRs per bit at the RLL encoder input $\{\lambda_i^{\mathsf{c}}\}$ in the following, i.e., we just consider one of the two RLL decoders depicted in Fig. 2.

For decoding we utilize the extended FSMs for joint (d,k) and NRZI encoding, which are introduced in Appendix B. The algorithm works on a time-invariant trellis, where the states at decoding time instance k' and transitions are denoted by $\tilde{s}_{k'} \in \tilde{\mathcal{S}}$ and $(\tilde{s}_{k'} = m, \tilde{s}_{k'+1} = m') \in \tilde{\mathcal{T}}$, respectively. Both are defined by the extended FSM RLL encoders (cf. Appendix B). We recall that the FSM RLL codes map codewords of p input bits onto codewords of q RLL symbols. Let $\boldsymbol{\sigma}(m,m') \in \{+1,-1\}^q$ denote the RLL output codeword in case of a transition $(m,m') \in \tilde{\mathcal{T}}$. Hence, the ith code bit at the input of the FSM RLL encoder can equivalently be denoted as the i'th bit in the k'th codeword of p bits at the encoder input, where $i' = 1 + \text{mod}(i-1, p)$ and $k' = 1 + \left\lfloor \frac{i-1}{p} \right\rfloor$. Then, following similar steps as in Section IV-B, we obtain the factorization of the joint probability

$$P\left(\tilde{s}_{k'-1}, \tilde{s}_{k'}, \left\{\lambda_l^{\mathsf{a}}\right\}\right) = \tilde{\alpha}\left(\tilde{s}_{k'-1}\right)\tilde{\gamma}_{k'}\left(\tilde{s}_{k'-1}, \tilde{s}_{k'}\right)\tilde{\beta}(\tilde{s}_{k'}), \tag{46}$$

where $\tilde{\gamma}_{k'}(\tilde{s}_{k'-1}, \tilde{s}_{k'})$ denotes the state transition probability and $\tilde{\alpha}(\tilde{s}_{k'})$ and $\tilde{\beta}(\tilde{s}_{k'})$ are defined through appropriately initialized forward and backward recursions, similar to (40) and (41). The a priori probabilities of the transitions can be omitted under the assumption that the bits c_i at the input of

the RLL encoder are independent and identically distributed (i.i.d.), because all valid transitions are equally probable in this case. Hence, the state transition probability $\tilde{\gamma}_{k'}(\tilde{s}_{k'-1}, \tilde{s}_{k'})$ is given by [42, Sec. II.C]

$$\tilde{\gamma}_{k'}\left(\tilde{s}_{k'-1} = m, \tilde{s}_{k'} = m'\right) = \prod_{i'=1}^{q}\left(1 + \exp\left(-\left[\boldsymbol{\sigma}(m, m')\right]_{i'} \cdot \lambda^{\mathsf{a}}_{i'+(k'-1)q}\right)\right)^{-1}, \quad (47)$$

where $[\boldsymbol{\sigma}(m, m')]_{i'}$ denotes the i'th element of $\boldsymbol{\sigma}(m, m')$. Note that the RHS of (47) corresponds to $P(\mathbf{a}_{k'} = \boldsymbol{\sigma}(m, m'))$. Finally, the output LLRs are obtained as

$$\lambda^{\mathsf{c}}_i = \log \frac{\sum_{(m,m')\in\tilde{\mathcal{T}}^{1}_{\mathsf{c},i'}} P\left(\tilde{s}_{k'-1} = m, \tilde{s}_{k'} = m', \{\lambda^{\mathsf{a}}_l\}\right)}{\sum_{(m,m')\in\tilde{\mathcal{T}}^{0}_{\mathsf{c},i'}} P\left(\tilde{s}_{k'-1} = m, \tilde{s}_{k'} = m', \{\lambda^{\mathsf{a}}_l\}\right)}, \quad (48)$$

where $\tilde{\mathcal{T}}^{1}_{\mathsf{c},i'}$ and $\tilde{\mathcal{T}}^{0}_{\mathsf{c},i'}$, $i' \in \{1, \ldots, p\}$, define the sets of state transition tuples $(\tilde{s}_{k'-1}, \tilde{s}_{k'})$ for which it holds that $\mathsf{c}_{i'+(k'-1)p} = 1$ and $\mathsf{c}_{i'+(k'-1)p} = 0$, respectively. A similar definition holds for λ^{d}_i with respect to d_i and the LLRs $\{\lambda^{\mathsf{b}}_l\}$.

1) COMPLEXITY

Similar to Section IV-B, we investigate the complexity of the RLL decoder in the remainder of this subsection. The number of trellis states $|\tilde{\mathcal{S}}|$ is given by $|\tilde{\mathcal{S}}| = 2|\bar{\mathcal{S}}|$, where $|\bar{\mathcal{S}}|$ denotes the number of states of the (d, k) sequence encoders provided in Tables 3 to 6. The factor two is due to extending the (d, k) encoders by NRZI encoding, which doubles the number of states. Furthermore, the number of transitions is given by $|\tilde{\mathcal{T}}| = 2^p|\tilde{\mathcal{S}}|$ because, by construction, every state has 2^p outgoing edges.

In the following, we evaluate the complexity in terms of the number of additions and multiplications, where the number of operations is normalized to the number of LLRs at the output. For simplicity, we treat divisions as multiplications again. Consequently, the normalized number of additions is given by $\tilde{N}_{\text{add}} = (1 + \frac{2+q}{p})|\tilde{\mathcal{T}}|$: The forward and backward recursions require $|\tilde{\mathcal{T}}|$ additions each and evaluating (47) requires q, all of which are only performed once for p subsequent LLRs at the output. Furthermore, evaluating (48) requires $|\tilde{\mathcal{T}}|$ additional additions due to $|\tilde{\mathcal{T}}^{1}_{\mathsf{c},i'}| + |\tilde{\mathcal{T}}^{0}_{\mathsf{c},i'}| = |\tilde{\mathcal{T}}|$. Then, computing (47) requires $\frac{3q-1}{p}|\tilde{\mathcal{T}}|$ normalized multiplications, $q - 1$ multiplications to compute the product and $2q$ multiplications to compute the factors, i.e., q for the inverse and q to evaluate the argument of the exponential function. Additionally, the forward and backward recursions together require $\frac{2}{p}|\tilde{\mathcal{T}}|$ normalized multiplications. Finally, evaluating (48) via (46) requires an additional $2|\tilde{\mathcal{T}}| + 1$ multiplications, where the single multiplication is due to the ratio. Hence, the normalized number of multiplications per LLR at the output is given by $\tilde{N}_{\text{mult}} = (2 + \frac{3q+1}{p})|\tilde{\mathcal{T}}| + 1$.

D. DISCUSSION

This subsection is dedicated to a discussion of the proposed transceiver design. In Section IV-A, we described a method to encode bits onto RLL sequences based on FSM encoders. Numerous alternative RLL encoding schemes are proposed in the literature; an overview can be found in [19, Sec. VI]. However, there is no widely accepted standard scheme. For example, the industry standard RLL codes for hard disk drives are a $(d = 1, k = 7)$ look-ahead encoder [35, Sec. 7.4], i.e., a state dependent block code, and a $(d = 2, k = 7)$ variable-length encoder [35, Sec. 7.3]. In order to avoid different encoding schemes and decoding algorithms for each RLL constraint, we focus on the class of fixed-length FSM RLL codes in this work. This facilitates adapting the code rate, as often required in wireless communications systems. Encoders for any desired RLL constraint can be derived using the ACH algorithm and the obtained encoders can provide a comparatively high coding-efficiency. Furthermore, the considered scheme has two additional advantages: *i*) the autocorrelation of the corresponding RLL sequence can be evaluated in closed form, as elaborated in Appendix B, and *ii*) it allows for a straightforward implementation of SISO decoding as detailed in Section IV-C.

The MAP RLL symbol detection equalizer proposed in Section IV-B is considered as a benchmark for practical equalization algorithms. In practice, the implementation complexity might be prohibitive, as evaluating the trellis state transition probabilities involves numerical integration and the number of trellis states can be huge. A performance comparison of different equalization algorithms for an AWGN channel is provided in [43]. Note that the modular receiver design, i.e., the division into equalizer and RLL decoder, facilitates employing a different equalizer.

Under *ideal* analog combining at the receiver, the in-phase and quadrature components are independent for the considered system model. Thus, the complexity of the equalizer could be reduced significantly by implementing separate equalization for the in-phase and quadrature components. However, this separation will likely not be valid in any practical system: Any mismatch in the correction of the phase-shifts due to the channel, e. g., when operating with finite-resolution phase shifters, results in a *complex* effective filter $\bar{v}(t)$ (cf. (13)) such that a separation is no longer valid.

For the equalizer, we obtain the a priori transition probabilities of the RLL sequence, i.e., $P(\mathsf{a}_l|\mathbf{a}^{l-1})$, from the corresponding maximum entropy RLL sequences (cf. Section II-B). Note that the *true* a priori probabilities when using the derived FSM RLL codes will be slightly different because the FSM RLL codes only approximate the underlying statistics of maximum entropy RLL sequences. This will result in a small mismatch in the a priori probabilities. However, as the FSM RLL codes closely approximate maximum entropy RLL sequences (cf. Table 2) and we observed only negligible performance gains when using the estimated actual transition probabilities, we use the maximum entropy transition probabilities for simplicity here.

The proposed receiver divides the operation into a soft-output equalizer, which provides soft-information per RLL

symbol, and a SISO RLL decoder converting this soft-information into reliability information per FEC encoded bit. In general, this separation is sub-optimal compared to a joint implementation. Yet, this division is practical as it allows to reduce the complexity of the equalizer: In a joint implementation the memory length of the equalizer is limited to multiples of the RLL encoder codeword length, i.e., to multiples of q. In this regard, note, e. g., that it holds $q = 8$ for $d = 4$ (cf. Section IV-A). An enhanced performance is expected when employing iterative receiver architectures. The evaluation of this is left for future work.

V. SPECTRAL EFFICIENCY LOWER BOUND

Based on the power spectral density (PSD) of the ZXM transmit signal provided in Section V-A and a lower bound on the achievable rate derived in Section V-B, we define a lower bound on the SE w. r. t. a fractional power containment bandwidth in Section V-C.

A. POWER SPECTRAL DENSITY

Due to linear modulation, $\mathsf{x}(t)$ is a *cyclostationary process* with period $\frac{T_\mathrm{N}}{M_\mathrm{Tx}}$ (cf. (4)). Consequently, the (average) PSD is given by [38, eq. (4-4-12)]

$$S_\mathsf{x}(f) = \frac{M_\mathrm{Tx}}{T_\mathrm{N}} S_\mathrm{RLL}(f)\,|F(f)|^2, \tag{49}$$

where $S_\mathrm{RLL}(f)$ and $F(f)$ denote the PSD of the RLL sequence and the frequency response, i.e., the Fourier transform, of the transmit filter $f(t)$, respectively. Employing the Wiener-Khinchin theorem, the PSD $S_\mathrm{RLL}(f)$ can be obtained as

$$S_\mathrm{RLL}(f) = \sum_{k=-\infty}^{\infty} R_\mathsf{x}[k]\, e^{-j2\pi f \frac{T_\mathrm{N}}{M_\mathrm{Tx}} k}, \tag{50}$$

where $R_\mathsf{x}[k]$ denotes the autocorrelation of the RLL symbol sequence $\mathbf{x}^m$. It is given by

$$\begin{aligned} R_\mathsf{x}[n] &= \mathbb{E}\{\mathsf{x}_l \mathsf{x}^*_{l+n}\} \overset{(a)}{=} \frac{1}{2}(\mathbb{E}\{\mathsf{a}_l \mathsf{a}_{l+n}\} + \mathbb{E}\{\mathsf{b}_l \mathsf{b}_{l+n}\}) \\ &\overset{(b)}{=} \mathbb{E}\{\mathsf{a}_l \mathsf{a}_{l+n}\} = R_\mathsf{a}[n], \end{aligned} \tag{51}$$

where (a) is due to (3) and due to the independence of $\mathbf{a}^m$ and $\mathbf{b}^m$, and (b) is due to identical statistics of $\mathbf{a}^m$ and $\mathbf{b}^m$. The autocorrelation of the RLL sequences generated by the FSM RLL codes derived in Section IV-A is computed in Appendix B, particularly, $R_\mathsf{a}[n]$ is given by (67).

Note that $S_\mathrm{RLL}(f)$, which is given in (50), is periodic in f with period $\frac{M_\mathrm{Tx}}{T_\mathrm{N}}$, i.e., the period increases with increasing M_Tx. An illustration of $S_\mathrm{RLL}(f)$ is provided in Fig. 5, where the PSD of the FSM RLL codes is compared to the PSD of maximum entropy RLL sequences (cf. Section II-B). It can be seen that the proposed choice of $d = M_\mathrm{Tx} - 1$ for ZXM results in a PSD which is well matched to the desired two-sided bandwidth of $\frac{1}{T_\mathrm{N}}$.

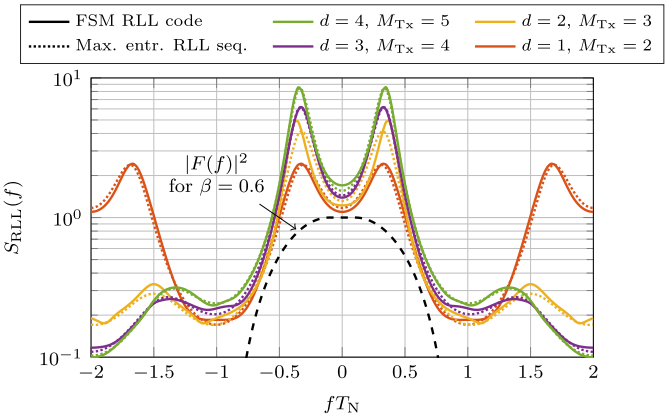

FIGURE 5. Comparison of the PSD $S_\mathrm{RLL}(f)$ of the derived FSM RLL codes to the PSD of the maxentropic RLL sequences from [35, Sec. 4.4.1]. Choosing $d = M_\mathrm{Tx} - 1$ results in a good match between $S_\mathrm{RLL}(f)$ and the desired band $f \in \left[-\frac{1}{2T_\mathrm{N}}, \frac{1}{2T_\mathrm{N}}\right]$. Note that $S_\mathrm{RLL}(f)$ is periodic with $\frac{M_\mathrm{Tx}}{T_\mathrm{N}}$ and that $S_\mathsf{x}(f)$ is obtained by multiplying $S_\mathrm{RLL}(f)$ with $|F(f)|^2$.

B. ACHIEVABLE RATE LOWER BOUND

In this section, we obtain a lower bound on the achievable rate of the presented system. Similar to [44], we evaluate the mutual information between a block of p bits at the input of the RLL encoder, denoted by $\mathbf{c}_{k'} = [\mathsf{c}_{1+(k'-1)p}, \ldots, \mathsf{c}_{k'p}]^T$, and the corresponding LLRs at the RLL decoder output, denoted by $\boldsymbol{\lambda}^\mathsf{c}_{k'} = [\lambda^\mathsf{c}_{1+(k'-1)p}, \ldots, \lambda^\mathsf{c}_{k'p}]^T$ (cf. Fig. 2). Hence, our goal is to evaluate

$$\lim_{K'\to\infty} \frac{1}{K'} I\big(\mathbf{c}_1, \ldots, \mathbf{c}_{K'}; \boldsymbol{\lambda}^\mathsf{c}_1, \ldots, \boldsymbol{\lambda}^\mathsf{c}_{K'}\big), \tag{52}$$

where $I(\cdot)$ denotes mutual information. For i.i.d. input bits c_i with $P(\mathsf{c}_i = 0) = P(\mathsf{c}_i = 1) = 0.5$, we obtain

$$\begin{aligned} &\frac{1}{K'} I\Big(\{\mathbf{c}_{k'}\}_{k'=1}^{K'}; \{\boldsymbol{\lambda}^\mathsf{c}_{k'}\}_{k'=1}^{K'}\Big) \\ &\quad\overset{(a)}{\geq} \frac{1}{K'} \sum_{k'=1}^{K'} \big(H(\mathbf{c}_{k'}) - H\big(\mathbf{c}_{k'} | \boldsymbol{\lambda}^\mathsf{c}_{k'}\big)\big) \qquad (53) \\ &\quad\overset{(b)}{=} H(\mathbf{c}_{k'}) - H\big(\mathbf{c}_{k'} | \boldsymbol{\lambda}^\mathsf{c}_{k'}\big) = I(\mathbf{c}_{k'}; \boldsymbol{\lambda}^\mathsf{c}_{k'}), \qquad (54) \end{aligned}$$

where (a) is due to the chain rule for entropy [45, Th. 2.5.1], due to the independence of the input bits c_i, and because conditioning cannot increase entropy [45, Th. 2.6.4]. Furthermore, (b) is due to identical statistics for all blocks. In the remainder of this section, we drop the index k'. Then, $I(\mathbf{c}; \boldsymbol{\lambda}^\mathsf{c})$ can be lower-bounded by

$$I(\mathbf{c}; \boldsymbol{\lambda}^\mathsf{c}) \overset{(a)}{\geq} \sum_{i=1}^{p} I\big(\mathsf{c}_i; \lambda^\mathsf{c}_i\big), \tag{55}$$

where (a) is due to the chain rule for entropy [45, Th. 2.5.1], due to c_i being i.i.d., and due to the fact that conditioning cannot increase entropy [45, Th. 2.6.5]. The RHS of (55) is achievable by BICM systems, because the FEC decoder performs parallel decoding of the bits, i.e., ignoring their dependencies [30], [44].

For i.i.d. input bits c_i, the RHS of (55) can be approximated numerically as [44]

$$\begin{aligned}\sum_{i=1}^{p} I\big(\mathsf{c}_i;\lambda_i^{\mathsf{c}}\big) &\overset{(a)}{=} \sum_{i=1}^{p} H(\mathsf{c}_i) - H\big(\mathsf{c}_i|\xi_i^{\mathsf{c}}\big)\\ &\overset{(b)}{=} p - \sum_{i=1}^{p}\sum_{b=0}^{1}\int_0^1 \frac{1}{2}\, f\big(\xi_i^{\mathsf{c}}|\mathsf{c}_i=b\big)\\ &\quad\times\ \log_2 \frac{f\big(\xi_i^{\mathsf{c}}\big)}{\frac{1}{2}\, f\big(\xi_i^{\mathsf{c}}|\mathsf{c}_i=b\big)}\,\mathrm{d}\,\xi_i^{\mathsf{c}}\\ &\overset{(c)}{\approx} p - \sum_{i=1}^{p}\sum_{b=0}^{1}\sum_{k=1}^{K}\frac{1}{2}\,\Xi_{i,k}^{b}\log_2\frac{\Xi_{i,k}^{0}+\Xi_{i,k}^{1}}{\Xi_{i,k}^{b}},\end{aligned} \tag{56}$$

where (a) is due to the fact that we can equivalently compute the mutual information between c_i and the bit probabilities

$$\xi_i^{\mathsf{c}} = \frac{1}{1+e^{-\lambda_i^{\mathsf{c}}}} \in [0,1], \tag{57}$$

because of a one-to-one mapping between λ_i^{c} and ξ_i^{c}. The remaining steps (b) and (c) follow from [44, eq. (9)] and [44, eq. (27)], respectively. The method employs Monte Carlo simulation to approximate the conditional bit probability distributions $f(\xi_i^{\mathsf{c}}|\mathsf{c}_i = b)$ through histograms with K uniformly distributed bins. The kth bin is therein denoted as $\Xi_{i,k}^{b}$. This approach is motivated by the fact that the conditional LLR distributions have infinite support, whereas the conditional bit probability distributions are limited to a finite range, which is more suitable for a numerical approximation through a histogram. Due to (56), a lower bound on the average mutual information per FEC encoded bit at the input of the FEC decoder is given by $\frac{1}{p}\sum_{i=1}^{p} I(\mathsf{c}_i;\lambda_i^{\mathsf{c}})$.

C. SPECTRAL EFFICIENCY LOWER BOUND

Here, we obtain a lower bound on the system's SE. We evaluate the SE w. r. t. a (one-sided) fractional power containment bandwidth W_Υ, which allows for $(1-\Upsilon)\times 100\,\%$ OOB emissions, with $\Upsilon \in (0,1]$. We define the fractional power containment bandwidth W_Υ as (cf. [46, eq. (2.23)])

$$\int_{-W_\Upsilon}^{W_\Upsilon} S_{\mathsf{x}}(f)\,\mathrm{d}f = \Upsilon\int_{-\infty}^{\infty} S_{\mathsf{x}}(f)\,\mathrm{d}f. \tag{58}$$

Hence, a SE lower bound w. r. t. W_Υ is obtained as

$$\mathrm{SE}_{\mathrm{LB}} = \frac{2\cdot M_{\mathrm{Tx}}\cdot R_{\mathrm{RLL}}\cdot\frac{1}{p}\sum_{i=1}^{p} I(\mathsf{c}_i;\lambda_i^{\mathsf{c}})}{2W_\Upsilon\cdot T_{\mathrm{N}}}\ [\mathrm{bit/s/Hz}], \tag{59}$$

where the factor 2 in the numerator is due to complex signaling. Recalling that the Nyquist bandwidth is given by $2W = \frac{1}{T_{\mathrm{N}}}$, we define the SNR as

$$\mathrm{SNR} = \frac{P}{2WN_0} \overset{(a)}{=} \frac{(E_{\mathrm{s}}\cdot M_{\mathrm{Tx}})/T_{\mathrm{N}}}{N_0/T_{\mathrm{N}}} = \frac{E_{\mathrm{s}}\cdot M_{\mathrm{Tx}}}{N_0}, \tag{60}$$

where P denotes the transmit power, (a) can be obtained from [47, Th. 18.3.2], and E_{s} denotes the energy per symbol, which is given by (cf. [47, eq. (18.20)])

$$E_{\mathrm{s}} = \frac{1}{m}\sum_{l=1}^{m}\sum_{l'=1}^{m} R_{\mathsf{x}}[l'-l]R_{\mathrm{ff}}\bigg((l'-l)\frac{T_{\mathrm{N}}}{M_{\mathrm{Tx}}}\bigg), \tag{61}$$

where $R_{\mathsf{x}}[n]$ denotes the autocorrelation of the complex RLL sequence, given in (51), and $R_{\mathrm{ff}}(\tau) = \int_{-\infty}^{\infty} f(t+\tau)f^*(t)\,\mathrm{d}\,t$ denotes the self-similarity function of the transmit filter $f(t)$ [47, Def. 11.2.1].

Besides, note that the relationship between SNR and $\frac{E_{\mathrm{b}}}{N_0}$, where E_{b} denotes the energy per information bit, is given by

$$\frac{E_{\mathrm{b}}}{N_0} = \frac{\mathrm{SNR}}{2\cdot M_{\mathrm{Tx}}\cdot R_{\mathrm{FEC}}\cdot R_{\mathrm{RLL}}}, \tag{62}$$

where R_{FEC} denotes the code rate of the FEC code. Note that for $M_{\mathrm{Tx}} = 1$, we do not employ RLL encoding, i.e., the RLL constraint is $(d=0, k=\infty)$, such that it holds $R_{\mathrm{RLL}} \equiv 1$.

VI. NUMERICAL RESULTS

In this section, we study the performance of the presented system numerically. First, we compare the implementation complexity of the proposed equalizer and the SISO RLL decoder in Section VI-A. Then, we evaluate the peak-to-average power ratio (PAPR) in Section VI-B. Afterwards, we investigate the SE lower bound, given by (59), and the coded performance in Section VI-C and Section VI-D, respectively. Finally, we evaluate the impact of the SWE in Section VI-E. Throughout this section we assume that the PSN *perfectly* compensates the phase-shifts due to the channel, i.e., we assume $\psi_n = \psi_n^{\mathrm{opt}}$ (cf. Section III-B).

A. COMPLEXITY EVALUATION

Here, we compare the complexity of the equalizer and the SISO RLL decoder numerically. We investigate the required number of additions and multiplications normalized to LLR tuples $(\lambda_l^{\mathsf{c}}, \lambda_l^{\mathsf{d}})$ at the output of the RLL decoders. Therefore, we scale the number of operations for the equalizer by $\frac{q}{p}$, to match the rates. Furthermore, we double the number of operations for the RLL decoder detailed in Section IV-C.1, because the system involves two parallel RLL decoders. The resulting complexity is depicted in Fig. 6 for $d \in \{1,\ldots,4\}$, where we always choose $M_{\mathrm{Tx}} = d+1$. For the equalizer we assume an increasing memory length with increasing d, such that $L \in \{4,6,8,10\}$, which mostly corresponds to the values used in Sections VI-C and VI-D for $M = 3$. Observing Fig. 6, we find that the equalizer complexity is roughly 10 times higher compared to the combined RLL decoder complexity. Moreover, we observe that the RLL decoder complexity is lowest for $d = 2$, which is due to the fact that the derived FSM RLL encoder for $d = 2$ has the fewest transitions (cf. Section IV-A). Note that the operations due to computing the trellis state transition probabilities in the equalizer are not taken into account, because they are assumed to be obtained offline, whereas their computation is taken into account for the RLL decoders.

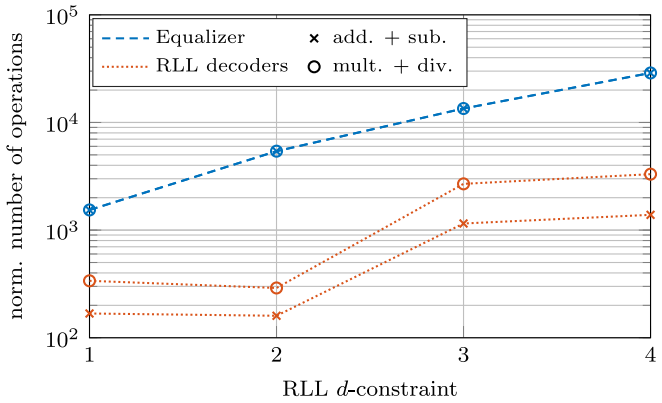

FIGURE 6. Number of receiver operations per LLR tuple $(\lambda_l^{\mathsf{c}}, \lambda_l^{\mathsf{d}})$ at the output of the RLL decoders (cf. Fig. 2). We choose $M_{\mathrm{Tx}} = d + 1$ and the memory length of the equalizer is given by $L \in \{4, 6, 8, 10\}$ for increasing d.

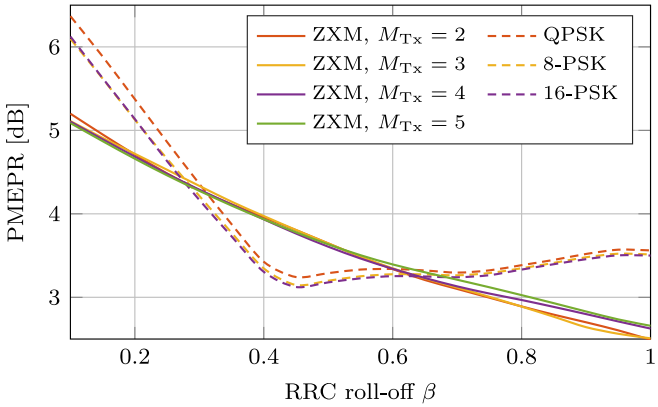

FIGURE 7. Evaluation of the PMEPR over the RRC roll-off for $d = M_{\mathrm{Tx}} - 1$.

B. PAPR EVALUATION

In this section, we evaluate the PAPR of the presented system. Investigating the PAPR of a specific modulation requires making assumptions on the carrier frequency, the bandwidth, and the signaling rate, as the PAPR is defined on the real-valued passband transmit signal [48]. To obtain more general insights, we evaluate the peak-to-mean-envelope power ratio (PMEPR) instead. The PMEPR can be understood as the baseband equivalent of the PAPR and it is defined as [49]

$$\mathrm{PMEPR}(\mathsf{x}(t)) = \frac{\max_t |\mathsf{x}(t)|^2}{\mathbb{E}\{|\mathsf{x}(t)|^2\}} \approx \frac{\max_{n \in \mathcal{N}_{\mathrm{eval}}} |\mathsf{x}(nT_{\mathrm{s}})|^2}{\frac{1}{N_{\mathrm{eval}}} \sum_{n=1}^{N_{\mathrm{eval}}} |\mathsf{x}(nT_{\mathrm{s}})|^2}, \tag{63}$$

where $\mathsf{x}(t)$ denotes the complex-valued transmit signal given in (4), $\mathcal{N}_{\mathrm{eval}} = \{1, \ldots, N_{\mathrm{eval}}\}$, and T_{s} and $N_{\mathrm{eval}} \in \mathbb{N}$ denote a sufficiently small sampling time interval and a large number of samples, respectively. For $f_{\mathrm{c}} \gg \frac{M_{\mathrm{Tx}}}{T_{\mathrm{N}}}$, where f_{c} denotes the carrier frequency, the relation between PAPR and PMEPR is given by [49, eq. (4)]

$$\mathrm{PAPR}(\mathsf{x}(t))\big|_{\mathrm{dB}} = \mathrm{PMEPR}(\mathsf{x}(t))\big|_{\mathrm{dB}} + 3\,\mathrm{dB}. \tag{64}$$

The PMEPR is evaluated for different RRC roll-off factors in Fig. 7. Parameters for the evaluation are chosen as $T_{\mathrm{s}} = \frac{T_{\mathrm{N}}}{100}$ and $N_{\mathrm{eval}} = 10^6$. In general, the PMEPR of the proposed ZXM implementation is in the same order of magnitude in dB compared to standard PSK. Furthermore, increasing M_{Tx} to values $M_{\mathrm{Tx}} > 2$ or increasing the constellation size for PSK has only a marginal impact on the PMEPR. For ZXM, the PMEPR is seen to decrease monotonically with the RRC roll-off factor β. As will be discussed in Section VI-C, for the ZXM system, a good choice for the RRC roll-off is $\beta = 0.6$, whereas, for a conventional PSK system, a typical choice would be $\beta_{\mathrm{PSK}} \in [0.2, 0.3]$. Hence, in practice, the PAPR of the presented ZXM system might be approx. 1.0 dB to 1.5 dB lower as compared to a conventional PSK system.

C. SPECTRAL EFFICIENCY EVALUATION

Here, we evaluate the SE lower bound w. r. t. a fractional power containment bandwidth W_Υ, given in (59). Numerical results are obtained by Monte Carlo simulation of 10^5 i. i. d. blocks $\mathbf{c}_{k'}$. The number of histogram bins to approximate the conditional bit probability distributions is chosen to $K = 256$. This corresponds to the choice of parameters utilized in [44]. The RRC filters $f(t)$ and $g(t)$ are truncated outside the interval $[-50T_{\mathrm{N}}, 50T_{\mathrm{N}}]$ to facilitate simulation. Furthermore, the effective memory length L of the auxiliary channel is chosen such that all coefficients with a magnitude of more than 15 % of the maximum are contained in $\bar{\mathbf{W}}$ (cf. Section III-D1). Moreover, we evaluate the performance for AoAs $\phi = \theta = 0$, which means there is no distortion due to the SWE, i.e., the evaluation in this subsection effectively corresponds to an evaluation over an AWGN channel. We also plot the SE, which corresponds to the capacity of an AWGN channel. For a fair comparison we define it as $\mathrm{SE}_{\mathrm{AWGN}}(\mathrm{SNR}) = \Upsilon^{-1} \log_2(1 + \mathrm{SNR})$, i.e., we allow for $(1 - \Upsilon) \times 100\,\%$ OOB emissions on the AWGN channel (cf. Section V-C).

First, we evaluate the effect of the choice of the RRC roll-off factor β on the SE lower bound w. r. t. three different fractional power containment bandwidths for $M_{\mathrm{Tx}} = 2$, d=1 and $M = 1$ in Fig. 8. The choice of the RRC roll-off factor represents a trade-off between PAPR, ISI, and bandwidth of the presented system. If we allow for a large amount of OOB emissions, e. g., when evaluating the performance w. r. t. $W_{90\%}$, a large roll-off maximizes the SE, i.e., $\beta = 0.7$ or $\beta = 0.9$. Vice versa, when evaluating the performance w. r. t. $W_{99\%}$, a small roll-off maximizes the SE, i.e., $\beta = 0.3$ or $\beta = 0.4$. In the remainder of this work, we always evaluate the performance w. r. t. $W_{95\%}$, i.e., we allow for 5 % OOB emissions, and always choose $\beta = 0.6$ for the ZXM system, because this choice maximizes the SE for SNR = 12.5 dB and yields a good performance for all considered configurations.

Second, we evaluate the effect of oversampling w. r. t. the signaling rate, i.e., the effect of increasing $M = \frac{M_{\mathrm{Rx}}}{M_{\mathrm{Tx}}}$, in

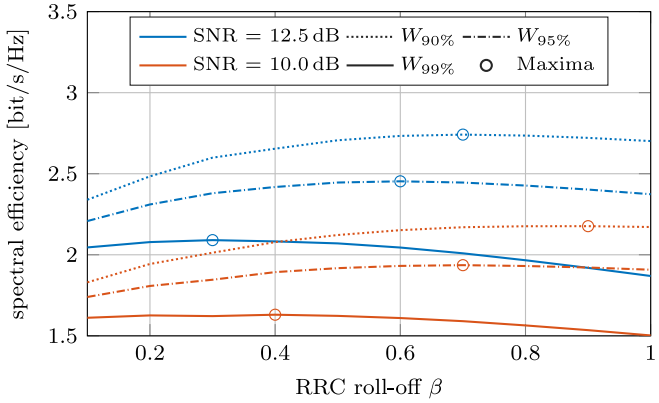

FIGURE 8. Evaluation of the SE lower bound for different RRC filter roll-offs w. r. t. different W_Υ for $M_{\mathrm{Tx}} = 2$, $d = 1$, and $M = 1$.

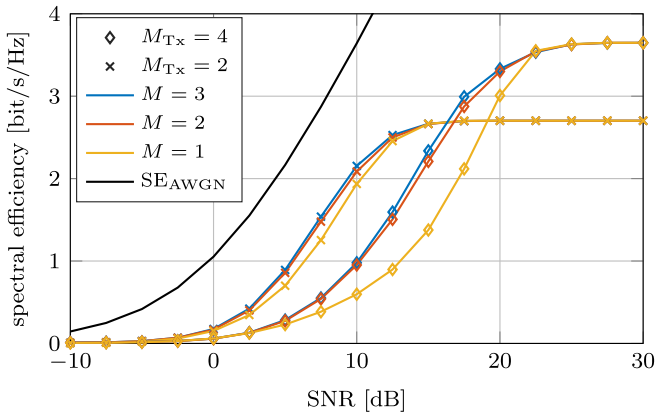

FIGURE 9. Evaluation of the SE lower bound for different $M = \frac{M_{\mathrm{Rx}}}{M_{\mathrm{Tx}}}$ w. r. t. $W_{95\%}$ for $d = M_{\mathrm{Tx}} - 1$ and $\beta = 0.6$.

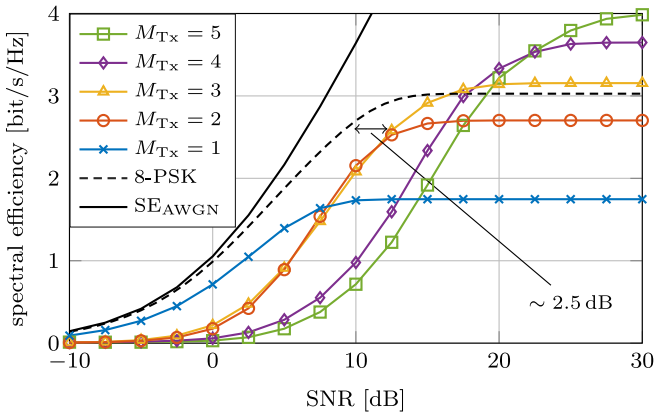

FIGURE 10. SE lower bound evaluation w. r. t. $W_{95\%}$. For the proposed system we chose $M = 3$, $d = M_{\mathrm{Tx}} - 1$, and $\beta = 0.6$. For the 8-PSK system we chose $\beta_{\mathrm{PSK}} = 0.25$ and assume an infinite ADC amplitude resolution.

Fig. 9. For SE $= 2$ bit/s/Hz, increasing M from 1 to 3 yields approx. 0.9 dB and approx. 3 dB gain for $M_{\mathrm{Tx}} = 2$ and $M_{\mathrm{Tx}} = 4$, respectively. However, most of the gain is already achieved by increasing M from 1 to 2. Note that the mismatch due to partly ignoring the noise correlation increases with M_{Tx}, whereas some of the correlation is captured for $M > 1$ (cf. Section IV-B).

Third, we evaluate the SE lower bound w. r. t. $W_{95\%}$ for different FTN signaling factors M_{Tx}, for $M = 3$ and $d = M_{\mathrm{Tx}} - 1$, in Fig. 10. It can be seen that standard QPSK, i.e., employing $M_{\mathrm{Tx}} = 1$ and $d = 0$, yields the highest SE at low SNR. With increasing SNR the highest SE is achieved with increasing M_{Tx}. The highest achieved SE is 4 bit/s/Hz with $M_{\mathrm{Tx}} = 5$. At SE $= 2.6$ bit/s/Hz, the presented ZXM system requires an approx. 2.5 dB higher SNR compared to a conventional 8-PSK system with a roll-off of $\beta_{\mathrm{PSK}} = 0.25$. However, note that we assume an *infinite* ADC amplitude resolution for the PSK system, while the ZXM system only employs 1-bit quantization. The SE of the 8-PSK system is evaluated numerically using [50].

Next, we compare the SE lower bound of the proposed transceiver design to lower bounds on the SE when omitting practical encoding and decoding schemes and when considering maximum entropy RLL sequences instead. Specifically, we compare the performance when evaluating the RHS of (55) while employing the derived FSM RLL codes to evaluating the LHS of (53) while employing maximum entropy RLL sequences. To this end, we follow the approach from [16], employ maximum entropy RLL transmit sequences (cf. Section II-B), and numerically evaluate the mutual information between long transmit sequences (10^5 RLL symbols) and the 1-bit quantized observations r_k (cf. Fig. 2) using the method from [51]. The numerical evaluation utilizes an auxiliary channel law and the forward recursion of the BCJR algorithm, which corresponds exactly to the forward recursion of the equalizer when employing the auxiliary channel, as described in Section IV-B and Section III-D1, respectively. The results are depicted in Fig. 11 for $\beta = 0.6$, $M = 1$, $d = M_{\mathrm{Tx}} - 1$ and an evaluation w. r. t. $W_{95\%}$. The saturation levels of the proposed practical system are at 94.4 % and 92.4 % of the saturation levels of the system employing maximum entropy RLL sequences, for $M_{\mathrm{Tx}} = 2$ and $M_{\mathrm{Tx}} = 4$, respectively. This corresponds roughly to the efficiencies of the utilized FSM RLL codes (cf. Table 2).[4] At SNR $= 12.5$ dB/22.5 dB the SE lower bound of the proposed implementation closely approximates the SE lower bound obtained for maximum entropy RLL sequences. However, at low SNR, the FSM RLL codes fail to achieve the performance, which is obtained by evaluating maximum entropy RLL sequences. The performance for the non-depicted configurations is similar. This suggests, that the presented implementation is sub-optimal and noise-sensitive. In practice, this observation is non-critical, as one would simply operate at a lower M_{Tx} (cf. Fig. 10). As an example, for SNR ≤ 7.5 dB, employing $M_{\mathrm{Tx}} = 1$, i.e., standard QPSK, yields a performance close to the performance of

4. Note that the efficiency η measures the efficiency in terms of rate, but does not take into account the slightly different bandwidth.

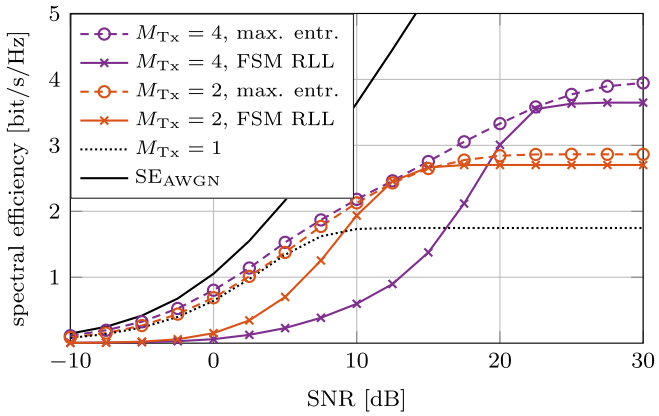

FIGURE 11. Evaluation of SE lower bounds w. r. t. $W_{95\%}$. Comparison of the proposed practical system to a theoretical system employing maximum entropy RLL transmit sequences with ideal demapping for $M = 1$, $d = M_{\mathrm{Tx}} - 1$, and $\beta = 0.6$.

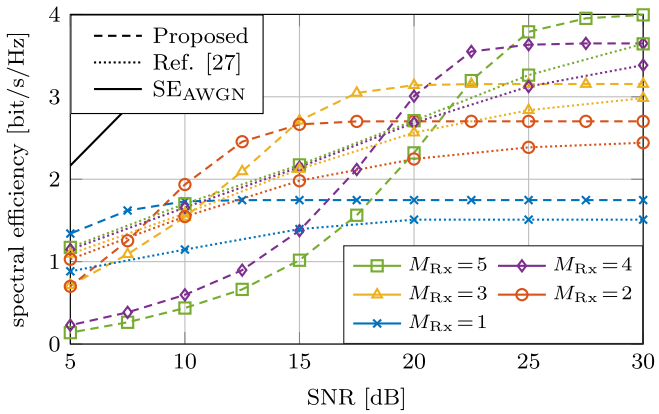

FIGURE 12. SE comparison to [27, Fig. 13] w. r. t. $W_{95\%}$, where the oversampling factor from [27] corresponds to M_{Rx} here. For the proposed system we choose $M = 1$, $d = M_{\mathrm{Tx}} - 1$, and $\beta = 0.6$.

maximum entropy RLL sequences at a significantly reduced complexity.

Finally, we compare the SE w. r. t. $W_{95\%}$ of the proposed system to a related system by *Deng et al.* from [27, Fig. 13], which also employs 1-bit quantization and temporal oversampling. Because [27] does not consider oversampling w. r. t. the signaling rate, we choose $M = 1$ for our system, such that the oversampling factor from [27] corresponds to M_{Rx} here. We compare ourselves to the non-uniform zero-crossing pattern, which allows for $M_{\mathrm{Rx}} + 1$ zero-crossings per Nyquist interval and achieves the highest SE of the schemes proposed in [27]. The comparison is depicted in Fig. 12 for $M = 1$, $d = M_{\mathrm{Tx}} - 1$, and $\beta = 0.6$. Over the whole considered SNR range, the highest SE is achieved by some configuration of the presented system. Notably, the gap to the AWGN capacity is significantly smaller for the proposed system, e. g., it is approx. 5.5 dB smaller at SE = 3 bit/s/Hz. When comparing the same M_{Rx} the difference is even larger. The SE saturation levels of the two schemes differ slightly.

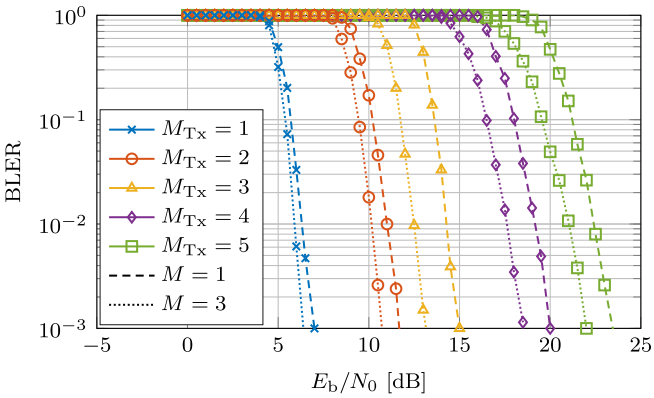

FIGURE 13. Block error rate of the presented system for $R_{\mathrm{FEC}} = 8/9$, $d = M_{\mathrm{Tx}} - 1$, and $\beta = 0.6$.

D. CODED PERFORMANCE EVALUATION

In this section, we evaluate the *coded* performance of the presented BICM system. To this aim, we employ the 5G NR LDPC code from the MATLAB 5G Toolbox as FEC scheme and subsequently perform random permutation interleaving across two subsequent codewords at the output of the FEC encoder. Furthermore, we choose base-graph 1 and an information word size of 1056 bits per LDPC codeword. For LDPC decoding, we employ the *normalized min-sum* (cf. [52]) algorithm with normalization factor 0.75 and a maximum of 20 iterations. Numerical results are obtained by simulating 10^4 blocks for each configuration.

First, we evaluate the BLER for $R_{\mathrm{FEC}} = 8/9$, $d = M_{\mathrm{Tx}} - 1$, and $\beta = 0.6$ in Fig. 13. It can be seen that the higher data rates due to increasing M_{Tx} require a larger $\frac{E_{\mathrm{b}}}{N_0}$ to achieve the same BLER, where E_{b} denotes the energy per information bit. Furthermore, the gain of oversampling w. r. t. the signaling rate is larger for higher values of M_{Tx}, i.e., increasing M from 1 to 3 yields 0.4 dB and 1.4 dB gain for $M_{\mathrm{Tx}} = 1$ and $M_{\mathrm{Tx}} = 5$, respectively.

Moreover, we evaluate the to the 95 % power containment bandwidth normalized *goodput*, i.e., the error-free application level throughput in bit/s/Hz, which we define as (cf. (59))

$$\mathrm{GP(SNR)} = \frac{2 \cdot M_{\mathrm{Tx}} \cdot R_{\mathrm{RLL}} \cdot R_{\mathrm{FEC}} \cdot (1 - \mathrm{BLER(SNR)})}{2 W_{95\%} \cdot T_{\mathrm{N}}}, \tag{65}$$

where BLER(SNR) can be obtained from Fig. 13 for $R_{\mathrm{FEC}} = 8/9$. The resulting goodput is depicted in Fig. 14 for $M = 1$, $d = M_{\mathrm{Tx}} - 1$, and $\beta = 0.6$. The evaluation indicates that it is beneficial to operate at very high FEC code rates before switching to a higher M_{Tx}. Furthermore, it can be seen that error-free transmission of more than 3.5 bit/s/Hz is possible with $M_{\mathrm{Tx}} = 5$ for SNRs above 27.5 dB.

E. EVALUATION OVER WIDEBAND LOS CHANNEL

In the previous sections, we have evaluated the performance for AoAs $\phi = \theta = 0°$, i.e., without any distortion due to the

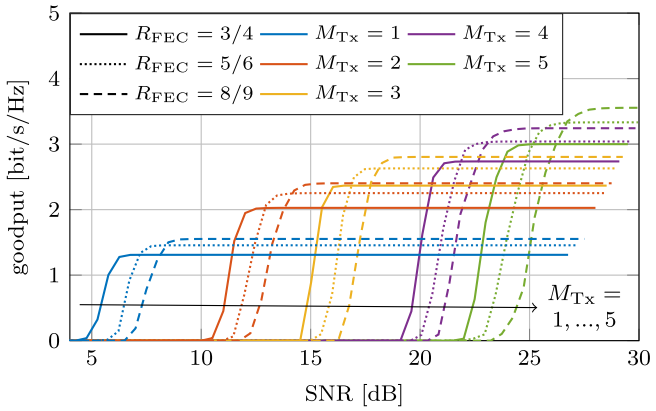

FIGURE 14. Evaluation of the goodput, i.e., the error-free application level throughput, normalized to $W_{95\%}$ for $M = 1$, $d = M_{\mathrm{Tx}} - 1$, and $\beta = 0.6$.

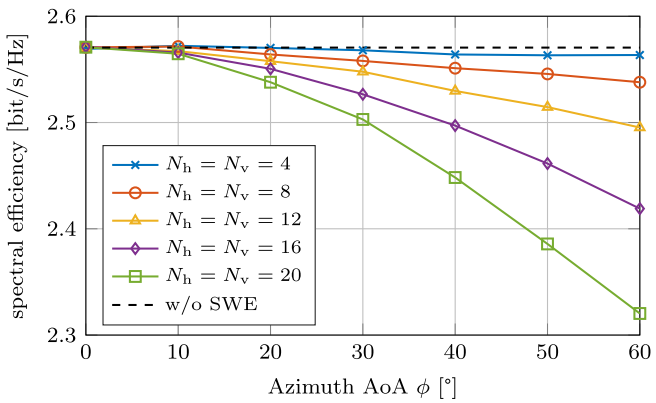

FIGURE 15. SE lower bound evaluation w. r. t. $W_{95\%}$ for a bandwidth-to-carrier-frequency ratio of $\frac{2W}{f_{\mathrm{c}}} = 0.1$ and for SNR $= 12.5$ dB, $M_{\mathrm{Tx}} = 3$, $M = 3$, $d = M_{\mathrm{Tx}} - 1$, and $\beta = 0.6$.

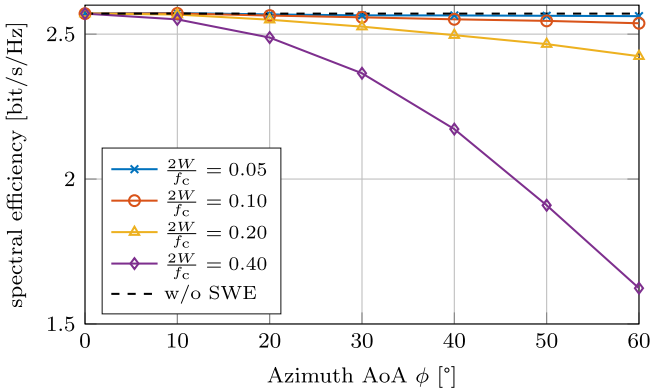

FIGURE 16. SE lower bound evaluation w. r. t. $W_{95\%}$ for $N_{\mathrm{h}} = N_{\mathrm{v}} = 8$, SNR $= 12.5$ dB, $M_{\mathrm{Tx}} = 3$, $M = 3$, $d = M_{\mathrm{Tx}} - 1$, and $\beta = 0.6$.

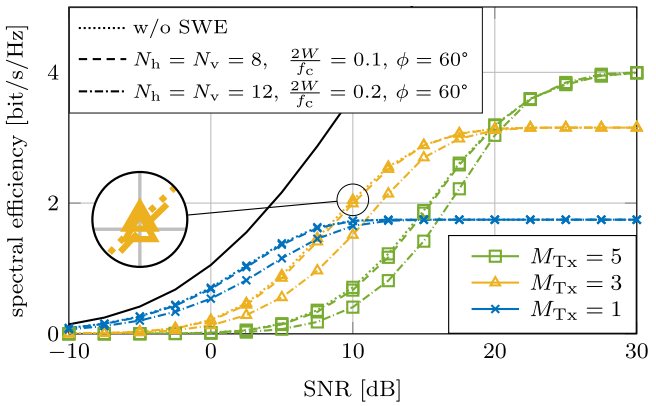

FIGURE 17. SE lower bound evaluation w. r. t. $W_{95\%}$ for $\theta = 0°$, $M = 3$, $d = M_{\mathrm{Tx}} - 1$, and $\beta = 0.6$.

SWE which results from physical propagation delays across the URA at the receiver [32]. Now, we consider an URA with a horizontal and vertical antenna spacing of $d_{\mathrm{h}} = \frac{\lambda_{\mathrm{c}}}{2}$ and $d_{\mathrm{v}} = \frac{\lambda_{\mathrm{c}}}{2}$, respectively, where λ_{c} denotes the wavelength which corresponds to the carrier frequency f_{c}. In the following, we fix the elevation AoA to $\theta = 0°$ and evaluate the SE lower bound for increasing azimuth AoA ϕ.

First, we compare the SE degradation due to the SWE for different URA sizes, where N_{h} and N_{v} denote the number of horizontal and vertical antennas, respectively. Note that the system model is normalized such that there is no beamforming gain, which facilitates studying the loss due to the SWE here. The SE lower bound w. r. t. $W_{95\%}$ is depicted in Fig. 15 for a bandwidth-to-carrier-frequency ratio of $\frac{2W}{f_{\mathrm{c}}} = 0.1$ and for SNR $= 12.5$ dB, $M_{\mathrm{Tx}} = 3$, $M = 3$, and $d = M_{\mathrm{Tx}} - 1$. The performance decreases with increasing URA size and azimuth AoA, because the delays and, hence, the incoherence increases. For sizes up to $N_{\mathrm{h}} = N_{\mathrm{v}} = 8$ the SE degradation is small, whereas it becomes significant for larger sizes.

Next, we compare the SE lower bound w. r. t. $W_{95\%}$ for different bandwidth-to-carrier-frequency ratios $\frac{2W}{f_{\mathrm{c}}}$ in Fig. 16. For this evaluation we choose $N_{\mathrm{h}} = N_{\mathrm{v}} = 8$, SNR $= 12.5$ dB, $M_{\mathrm{Tx}} = 3$, $M = 3$, and $d = M_{\mathrm{Tx}} - 1$. A significant performance degradation is observed for high azimuth AoAs and $\frac{2W}{f_{\mathrm{c}}} > 0.1$. However, for $\frac{2W}{f_{\mathrm{c}}} \leq 0.1$ the SE degradation is comparatively small for all considered AoAs.

Finally, in Fig. 17, we evaluate the impact of the SWE when varying the FTN signaling factor M_{Tx} over the SNR for $M = 3$, $d = M_{\mathrm{Tx}} - 1$, and $\beta = 0.6$. We evaluate the performance for a high AoA of $\phi = 60°$. For $N_{\mathrm{h}} = N_{\mathrm{v}} = 8$ and $\frac{2W}{f_{\mathrm{c}}} = 0.1$ the loss is found to be marginal. In contrast, for $N_{\mathrm{h}} = N_{\mathrm{v}} = 12$ and $\frac{2W}{f_{\mathrm{c}}} = 0.2$ a significant loss is observed, e. g., the loss is approx. 2 dB at SE $= 2$ bit/s/Hz for $M_{\mathrm{Tx}} = 3$. However, for the considered configurations, the SE saturation level is not affected. The performance of the non-depicted FTN signaling factors, i.e., $M_{\mathrm{Tx}} = 2$ and $M_{\mathrm{Tx}} = 4$, is similar. Furthermore, the loss due to the SWE does not increase with M_{Tx} for the investigated parameters.

The findings above indicate that employing low-cost PSNs, i.e., employing narrowband analog combining at the receiver, results only in a marginal loss for antenna array sizes of up to $N_{\mathrm{h}} = N_{\mathrm{v}} = 8$ and bandwidth-to-carrier-frequency ratios up to $\frac{2W}{f_{\mathrm{c}}} = 0.1$. For larger antenna array sizes or bandwidth-to-carrier-frequency ratios it might be

TABLE 3. FSM encoder for $(d = 1, k = \infty)$ with $R_{\text{RLL}} = 2/3$.

Cur. state	Input	Output	Next state	Cur. state	Input	Output	Next state
1	00	001	1	3	00	010	2
	01	010	2		01	010	3
	10	000	3		10	101	1
	11	010	3		11	001	1
2	00	100	2				
	01	000	3				
	10	100	3				
	11	000	2				

TABLE 4. FSM encoder for $(d = 2, k = \infty)$ with $R_{\text{RLL}} = 1/2$.

Cur. state	Input	Output	Next state	Cur. state	Input	Output	Next state
1	0	00	3	3	0	01	1
	1	00	4		1	10	2
2	0	01	1	4	0	00	3
	1	00	3		1	00	4

necessary to implement *wideband* analog combining, i.e., utilizing true-time delays or the approach proposed in [53]. Evaluating the performance for finite-resolution PSNs is left for future work.

VII. CONCLUSION

In this work, we proposed a practical zero-crossing modulation (ZXM) transceiver design, which combines faster-than-Nyquist (FTN) signaling and runlength-limited (RLL) transmit sequences, for a system employing 1-bit quantization and oversampling at the receiver. We derived four fixed-length FSM RLL encoders enabling efficient transmit signal generation and soft-demapping at the receiver. Our numerical results indicate that the presented system has an up to 1.5 dB lower PAPR than conventional PSK systems at the envisioned operating point. Moreover, we showed that SEs of 4 bit/s/Hz, and, with practical channel codes, error-free transmission of up to 3.5 bit/s/Hz, are achievable. Furthermore, our numerical results suggest that the loss due to narrowband analog combining at the receiver is small for many practical configurations, e. g., for an antenna array size of 8×8 and a bandwidth-to-carrier-frequency ratio of 10 %.

Although we showed that the presented transceiver design closely approximates the performance predicted in [16] at sufficiently high SNR, there is still a significant loss at low SNR (cf. Fig. 11). This loss could be related to the difference between the mutual information on the LHS of (53) and the RHS of (55). In practice, most of this low SNR loss can be mitigated by adaptively choosing the FTN signaling factor and the RLL constraint, which is also beneficial in terms of complexity (cf. Fig. 6). Nevertheless, investigating alternative bit mappings, i.e., alternative RLL encoding schemes, and coded modulation approaches, e. g., multi-level coding [54], is an open research direction.

APPENDIX A
DERIVED FSM RLL CODES

In this section, we present the derived FSM (d, k) encoders in Tables 3 to 6. The encoders were derived using the ACH [39] or state-splitting algorithm [40, Ch. 5] (cf. Section IV-A). Inputs and outputs are read from left-to-right.

TABLE 5. FSM encoder for $(d = 3, k = \infty)$ with $R_{\text{RLL}} = 3/7$.

Cur. state	Input	Output	Next state	Cur. state	Input	Output	Next state
1	000	0001000	6	6	000	1000000	6
	001	0000100	4		001	0000000	6
	010	0000010	2		010	0010000	8
	011	0000001	1		011	1000010	2
	100	0000000	6		100	0100001	1
	101	0001000	8		101	1000010	3
	110	0000000	8		110	1000000	7
	111	0000010	3		111	0000000	7
2	000	0010000	6	7	000	0010000	6
	001	0000100	4		001	1000000	8
	010	0000000	6		010	0000000	8
	011	0001000	8		011	1000001	1
	100	0010001	1		100	0000010	2
	101	0000100	5		101	0000010	3
	110	0010000	7		110	0010000	7
	111	0000000	7		111	1000000	9
3	000	0001000	6	8	000	0100000	8
	001	0000010	2		001	0100000	6
	010	0010000	8		010	1000100	4
	011	0000000	8		011	0100010	2
	100	0000001	1		100	0000001	1
	101	0000010	3		101	1000100	5
	110	0001000	7		110	0100000	7
	111	0010000	9		111	0100000	9
4	000	0100000	6	9	000	0001000	8
	001	0001000	6		001	0001000	6
	010	0000000	6		010	0000100	4
	011	0010000	8		011	0010001	1
	100	0000000	8		100	0100010	3
	101	0010001	1		101	0000100	5
	110	0000001	1		110	0001000	7
	111	0000010	3		111	0001000	9
5	000	0010000	6				
	001	0000100	4				
	010	0100000	8				
	011	0001000	8				
	100	0100010	2				
	101	0100001	1				
	110	0000010	2				
	111	0100010	3				

APPENDIX B
AUTOCORRELATION OF FSM RLL CODES

In this section, we elaborate on how to compute the autocorrelation of the FSM RLL codes detailed in Appendix A by following similar steps as in [35, Sec. 3.5]. First, the FSM RLL code definitions from Tables 3 to 6, are extended to also include NRZI encoding: Each state in the original FSM corresponds to two states in the *extended* FSM, where one is associated with the amplitude $+1$ at the beginning of the block and the other with the amplitude -1. Then, the outputs of the FSM codes, which are in the form of (d, k) sequences, are NRZI encoded, starting with the amplitude associated with the current state, i.e., ± 1. Finally, the *next state* is updated, such that it matches the amplitude of the last RLL symbol in the *output* sequence. An example for the derived $(d = 2, k = \infty)$ code, given in Table 4, is provided in Table 7, where inputs and outputs are read from left to right. Note that Table 7 also defines

TABLE 6. FSM encoder for $(d = 4, k = \infty)$ with $R_{\mathrm{RLL}} = 3/8$.

Cur. state	Input	Output	Next state	Cur. state	Input	Output	Next state
1	000	00001000	5	6	000	00100000	7
	001	00000100	3		001	00001000	5
	010	00000010	2		010	01000000	9
	011	00000001	1		011	00010000	9
	100	00000000	7		100	01000010	2
	101	00000000	9		101	01000001	1
	110	00000100	4		110	00000100	3
	111	00001000	6		111	00000001	1
2	000	00010000	7	7	000	10000000	7
	001	00001000	5		001	00000000	7
	010	00000100	3		010	00100000	9
	011	00000010	2		011	00000100	3
	100	00000001	1		100	01000001	1
	101	00000000	7		101	00000100	4
	110	00010000	9		110	10000000	8
	111	00000000	9		111	00000000	8
3	000	00100000	7	8	000	00100000	7
	001	00001000	5		001	10000000	9
	010	00000000	7		010	00000000	9
	011	00010000	9		011	10000001	1
	100	00100001	1		100	00000010	2
	101	00000001	1		101	00100000	8
	110	00001000	6		110	10000000	10
	111	00100000	8		111	00000000	10
4	000	00010000	7	9	000	01000000	9
	001	00000100	3		001	01000000	7
	010	00100000	9		010	10000100	3
	011	00000000	9		011	10000010	2
	100	00000010	2		100	00100001	1
	101	00000100	4		101	10000100	4
	110	00010000	8		110	01000000	8
	111	00100000	10		111	01000000	10
5	000	01000000	7	10	000	00010000	9
	001	00010000	7		001	00010000	7
	010	00000000	7		010	00001000	5
	011	00100000	9		011	01000010	2
	100	00000000	9		100	00000001	1
	101	00100001	1		101	00001000	6
	110	00000010	2		110	00010000	8
	111	00000100	4		111	00010000	10

the sets of states and transitions, i.e., $\tilde{\mathcal{S}}$ and $\tilde{\mathcal{T}}$, respectively (cf. Section IV-C). Afterwards, the resulting FSMs for joint (d, k) and NRZI encoding, which are provided in the form of *Mealy* machines [55], have to be converted to equivalent *Moore* machines [56]. Note that Mealy machines associate the output with the current state *and* input, whereas Moore machines associate the output only with the current state. An example for an equivalent Moore machine to the extended Mealy machine in Table 7 is provided in Table 8, where inputs and outputs are again read from left to right.

Let $\mathbf{Q} \in \mathbb{R}^{\Omega\times\Omega}$ denote the state transition probability matrix of the equivalent Moore machine, where Ω denotes the number of states. Note that for i. i. d. input bits, all valid state transitions are equally probable. Then, we denote the stationary distribution of the equivalent Moore machine by $\boldsymbol{\pi} \in \mathbb{R}^{\Omega}$, i.e., it holds $\boldsymbol{\pi}^T\mathbf{Q} = \boldsymbol{\pi}^T$. Furthermore, we define an output matrix $\boldsymbol{\Gamma} \in \mathbb{R}^{\Omega\times q}$ where the nth row is defined such that it contains the Moore machine's output in state n. For example, when considering the code in Table 8, the matrix $\boldsymbol{\Gamma}$ corresponds to the column *output*. Then, the block-wise correlation matrix of the FSM RLL encoder output is given

TABLE 7. Extended FSM encoder for joint (d, k) and NRZI encoding, derived from the (d, k) encoder defined in Table 4.

Current state	Input	Output	Next state
1_+	0	$+1+1$	3_+
	1	$+1+1$	4_+
2_+	0	$+1-1$	1_-
	1	$+1+1$	3_+
3_+	0	$+1-1$	1_-
	1	$-1-1$	2_-
4_+	0	$+1+1$	3_+
	1	$+1+1$	4_+
1_-	0	$-1-1$	3_-
	1	$-1-1$	4_-
2_-	0	$-1+1$	1_+
	1	$-1-1$	3_-
3_-	0	$-1+1$	1_+
	1	$+1+1$	2_+
4_-	0	$-1-1$	3_-
	1	$-1-1$	4_-

TABLE 8. Equivalent Moore machine for Mealy machine from Table 7.

Current state	Next state for input 0	Next state for input 1	Output
1'	3'	4'	$-1+1$
2'	5'	3'	$+1+1$
3'	5'	6'	$+1+1$
4'	3'	4'	$+1+1$
5'	7'	8'	$+1-1$
6'	1'	7'	$-1-1$
7'	1'	2'	$-1-1$
8'	7'	8'	$-1-1$

by [35, eq. (3.46)]

$$\mathbf{R}_{\mathsf{a}}^{k} = \mathbb{E}\left\{\mathbf{a}_{k'}\mathbf{a}_{k'+k}^{T}\right\} = \boldsymbol{\Gamma}^{T}\boldsymbol{\Pi}\mathbf{Q}^{|k|}\boldsymbol{\Gamma}, \tag{66}$$

where $\boldsymbol{\Pi} = \mathrm{diag}(\boldsymbol{\pi})$ and $\mathbf{a}_{k'}^{T} = [\mathsf{a}_{1+(k'-1)q}, \ldots, \mathsf{a}_{k'q}]$ denotes the k'th codeword in a sequence of codewords at the output of the FSM RLL encoder. Finally, the scalar autocorrelation $R_{\mathsf{a}}[n] = \mathbb{E}\{\mathsf{a}_l\mathsf{a}_{l+n}\}$ of the RLL sequence at the output of the encoder can be obtained as [35, eq. (3.39)]

$$R_{\mathsf{a}}[kq+l] = \frac{1}{q}\left(\sum_{i=1}^{q-l}\left[\mathbf{R}_{\mathsf{a}}^{k}\right]_{i,l+i} + \sum_{i=q-l+1}^{q}\left[\mathbf{R}_{\mathsf{a}}^{k+1}\right]_{i,l+i-q}\right), \tag{67}$$

for $k \in \mathbb{Z}$, $0 \le l \le q-1$.

ACKNOWLEDGMENT

The authors thank H. Halbauer, V. Braun, S. Wesemann, L. T. N. Landau, M. Schlüter, S. Zeitz, F. Gast, and M. Shang for insightful discussions of this work. Computations were performed at the Center for Information Services and High Performance Computing (ZIH) at Technische Universität Dresden.

REFERENCES

[1] P. Neuhaus *et al.*, "Sub-THz wideband system employing 1-bit quantization and temporal oversampling," in *Proc. IEEE Int. Conf. Commun. (ICC)*, Dublin, Ireland, Jun. 2020, pp. 1–7.

[2] P. Neuhaus, M. Dörpinghaus, H. Halbauer, V. Braun, and G. Fettweis, "On the spectral efficiency of oversampled 1-bit quantized systems for wideband LOS channels," in *Proc. IEEE Int. Symp. Pers. Indoor Mobile Radio Commun. (PIMRC)*, London, U.K., Aug. 2020, pp. 1–6.

[3] T. S. Rappaport *et al.*, "Wireless communications and applications above 100 GHz: Opportunities and challenges for 6G and beyond," *IEEE Access*, vol. 7, pp. 78729–78757, 2019.

[4] R. W. Heath, N. González-Prelcic, S. Rangan, W. Roh, and A. M. Sayeed, "An overview of signal processing techniques for millimeter wave MIMO systems," *IEEE J. Sel. Areas Commun.*, vol. 10, no. 3, pp. 436–453, Apr. 2016.

[5] B. Murmann. *ADC Performance Survey 1997–2020*. Accessed: Aug. 2020. [Online]. Available: https://web.stanford.edu/~murmann/adcsurvey.html

[6] T. Sundstrom, B. Murmann, and C. Svensson, "Power dissipation bounds for high-speed Nyquist analog-to-digital converters," *IEEE Trans. Circuits Syst. I, Reg. Papers*, vol. 56, no. 3, pp. 509–518, Mar. 2009.

[7] R. B. Staszewski, "Digitally intensive wireless transceivers," *IEEE Des. Test Comput.*, vol. 29, no. 6, pp. 7–18, Dec. 2012.

[8] S. Ziabakhsh, G. Gagnon, and G. W. Roberts, "The peak-SNR performances of voltage-mode versus time-mode circuits," *IEEE Trans. Circuits Syst. II, Exp. Briefs*, vol. 65, no. 12, pp. 1869–1873, Dec. 2018.

[9] E. N. Gilbert, "Increased information rate by oversampling," *IEEE Trans. Inf. Theory*, vol. 39, no. 6, pp. 1973–1976, Nov. 1993.

[10] S. Shamai, "Information rates by oversampling the sign of a bandlimited process," *IEEE Trans. Inf. Theory*, vol. 40, no. 4, pp. 1230–1236, Jul. 1994.

[11] T. Koch and A. Lapidoth, "Increased capacity per unit-cost by oversampling," in *Proc. IEEE Convers. Elect. Electron. Eng. Israel (IEEEI)*, Eliat, Israel, Nov. 2010, pp. 684–688.

[12] W. Zhang, "A general framework for transmission with transceiver distortion and some applications," *IEEE Trans. Commun.*, vol. 60, no. 2, pp. 384–399, Feb. 2012.

[13] S. Bender, M. Dörpinghaus, and G. Fettweis, "On the achievable rate of bandlimited continuous-time 1-bit quantized AWGN channels," in *Proc. IEEE Int. Symp. Inf. Theory (ISIT)*, Aachen, Germany, Jun. 2017, pp. 2083–2087.

[14] S. Bender, M. Dörpinghaus, and G. P. Fettweis, "On the achievable rate of bandlimited continuous-time AWGN channels with 1-bit output quantization," *EURASIP J. Wireless Commun. Netw.*, vol. 2021, no. 1, p. 54, Mar. 2021.

[15] G. Fettweis, M. Dörpinghaus, S. Bender, L. Landau, P. Neuhaus, and M. Schlüter, "Zero crossing modulation for communication with temporally oversampled 1-bit quantization," in *Proc. Asilomar Conf. Signals Syst. Comput.*, Pacific Grove, CA, USA, Nov. 2019, pp. 207–214.

[16] L. T. N. Landau, M. Dörpinghaus, and G. P. Fettweis, "1-bit quantization and oversampling at the receiver: Sequence-based communication," *EURASIP J. Wireless Commun. Netw.*, vol. 2018, no. 1, p. 83, Apr. 2018.

[17] L. Landau, M. Dörpinghaus, and G. Fettweis, "Communications employing 1-bit quantization and oversampling at the receiver: Faster-than-Nyquist signaling and sequence design," in *Proc. IEEE Int. Conf. Ubiquitous Wireless Broadband (ICUWB)*, Montreal, QC, Canada, Oct. 2015, pp. 1–5.

[18] J. E. Mazo, "Faster-than-Nyquist signaling," *Bell Syst. Tech. J.*, vol. 54, no. 8, pp. 1451–1462, Oct. 1975.

[19] K. A. S. Immink, "Runlength-limited sequences," *Proc. IEEE*, vol. 78, no. 11, pp. 1745–1759, Nov. 1990.

[20] L. Landau, M. Dörpinghaus, and G. P. Fettweis, "1-bit quantization and oversampling at the receiver: Communication over bandlimited channels with noise," *IEEE Commun. Lett.*, vol. 21, no. 5, pp. 1007–1010, May 2017.

[21] S. Bender, M. Dörpinghaus, and G. Fettweis, "On the spectral efficiency of bandlimited 1-bit quantized AWGN channels with runlength-coding," *IEEE Commun. Lett.*, vol. 24, no. 10, pp. 2147–2151, Oct. 2020.

[22] L. T. N. Landau, M. Dörpinghaus, R. C. de Lamare, and G. P. Fettweis, "Achievable rate with 1-bit quantization and oversampling using continuous phase modulation-based sequences," *IEEE Trans. Wireless Commun.*, vol. 17, no. 10, pp. 7080–7095, Oct. 2018.

[23] A. Gokceoglu, E. Björnson, E. G. Larsson, and M. Valkama, "Spatio-temporal waveform design for multiuser massive MIMO downlink with 1-bit receivers," *IEEE J. Sel. Topics Signal Process.*, vol. 11, no. 2, pp. 347–362, Mar. 2017.

[24] D. M. V. Melo, L. T. N. Landau, and R. C. de Lamare, "Zero-crossing precoding with maximum distance to the decision threshold for channels with 1-bit quantization and oversampling," in *Proc. IEEE Int. Conf. Acoust. Speech Signal Process. (ICASSP)*, Barcelona, Spain, May 2020, pp. 5120–5124.

[25] D. M. V. Melo, L. T. N. Landau, and R. C. de Lamare, "Zero-crossing precoding with MMSE criterion for channels with 1-bit quantization and oversampling," in *Proc. Int. ITG Workshop Smart Antennas (WSA)*, Hamburg, Germany, Feb. 2020, pp. 1–6.

[26] A. B. Üçüncü and A. Ö. Yılmaz, "Oversampling in one-bit quantized massive MIMO systems and performance analysis," *IEEE Trans. Wireless Commun.*, vol. 17, no. 12, pp. 7952–7964, Dec. 2018.

[27] R. Deng, J. Zhou, and W. Zhang, "Bandlimited communication with one-bit quantization and oversampling: Transceiver design and performance evaluation," *IEEE Trans. Commun.*, vol. 69, no. 2, pp. 845–862, Feb. 2021.

[28] Y. Jeon, H. Do, S. Hong, and N. Lee, "Soft-output detection methods for sparse millimeter-wave MIMO systems with low-precision ADCs," *IEEE Trans. Commun.*, vol. 67, no. 4, pp. 2822–2836, Apr. 2019.

[29] E. Zehavi, "8-PSK trellis codes for a Rayleigh channel," *IEEE Trans. Commun.*, vol. 40, no. 5, pp. 873–884, May 1992.

[30] G. Caire, G. Taricco, and E. Biglieri, "Bit-interleaved coded modulation," *IEEE Trans. Inf. Theory*, vol. 44, no. 3, pp. 927–946, May 1998.

[31] S. Buzzi, C. D'Andrea, T. Foggi, A. Ugolini, and G. Colavolpe, "Single-carrier modulation versus OFDM for millimeter-wave wireless MIMO," *IEEE Trans. Commun.*, vol. 66, no. 3, pp. 1335–1348, Mar. 2018.

[32] B. Wang, F. Gao, S. Jin, H. Lin, and G. Y. Li, "Spatial- and frequency-wideband effects in millimeter-wave massive MIMO systems," *IEEE Trans. Signal Process.*, vol. 66, no. 13, pp. 3393–3406, Jul. 2018.

[33] X. Song, S. Haghighatshoar, and G. Caire, "Efficient beam alignment for millimeter wave single-carrier systems with hybrid MIMO transceivers," *IEEE Trans. Wireless Commun.*, vol. 18, no. 3, pp. 1518–1533, Mar. 2019.

[34] *NR; Multiplexing and Channel Coding, Release 16*, 3GPP Standard TS 38.212, Dec. 2019.

[35] K. A. S. Immink, *Codes for Mass Data Storage Systems*. Eindhoven, The Netherlands: Shannon Found., 2004.

[36] M. Schlüter, M. Dörpinghaus, and G. P. Fettweis, "Bounds on phase, frequency, and timing synchronization in fully digital receivers with 1-bit quantization and oversampling," *IEEE Trans. Commun.*, vol. 68, no. 10, pp. 6499–6513, Oct. 2020.

[37] H. L. Van Trees, *Optimum Array Processing: Part IV of Detection, Estimation, and Modulation Theory*. New York, NY, USA: Wiley, 2002.

[38] J. G. Proakis, *Digital Communications*. New York, NY, USA: McGraw-Hill, 1995.

[39] R. Adler, D. Coppersmith, and M. Hassner, "Algorithms for sliding block codes—An application of symbolic dynamics to information theory," *IEEE Trans. Inf. Theory*, vol. IT-29, no. 1, pp. 5–22, Jan. 1983.

[40] B. H. Marcus, R. M. Roth, and P. H. Siegel. (2001). *An Introduction to Coding for Constrained Systems*, Lecture Notes. [Online]. Available: https://www.math.ubc.ca/~marcus/Handbook/index.html

[41] L. Bahl, J. Cocke, F. Jelinek, and J. Raviv, "Optimal decoding of linear codes for minimizing symbol error rate (corresp.)," *IEEE Trans. Inf. Theory*, vol. IT-20, no. 2, pp. 284–287, Mar. 1974.

[42] M. Tüchler and A. C. Singer, "Turbo equalization: An overview," *IEEE Trans. Inf. Theory*, vol. 57, no. 2, pp. 920–952, Feb. 2011.

[43] S. Zeitz, P. Neuhaus, M. Schlüter, M. Dörpinghaus, and G. Fettweis, "Soft-output equalizers for systems employing 1-bit quantization and temporal oversampling," in *Proc. IEEE Wireless Commun. Netw. Conf. (WCNC)*, Nanjing, China, Mar. 2021, pp. 1–6.

[44] P. Fertl, J. Jalden, and G. Matz, "Performance assessment of MIMO-BICM demodulators based on mutual information," *IEEE Trans. Signal Process.*, vol. 60, no. 3, pp. 1366–1382, Mar. 2012.

[45] T. M. Cover and J. A. Thomas, *Elements of Information Theory*. New York, NY, USA: Wiley, 2006.

[46] U. Madhow, *Fundamentals of Digital Communication*. Cambridge, U.K.: Cambridge Univ. Press, 2008.

[47] A. Lapidoth, *A Foundation in Digital Communication*. Cambridge, U.K.: Cambridge Univ. Press, 2017.

[48] S. Litsyn, *Peak Power Control in Multicarrier Communications*. Cambridge, U.K.: Cambridge Univ. Press, 2007.

[49] S. Daumont, B. Rihawi, and Y. Lout, "Root-raised cosine filter influences on PAPR distribution of single carrier signals," in *Proc. Int. Symp. Commun. Control Signal Process.*, St Julian's, Malta, Mar. 2008, pp. 841–845.
[50] G. Ungerboeck, "Channel coding with multilevel/phase signals," *IEEE Trans. Inf. Theory*, vol. IT-28, no. 1, pp. 55–67, Jan. 1982.
[51] D. M. Arnold, H. A. Loeliger, P. O. Vontobel, A. Kavcic, and W. Zeng, "Simulation-based computation of information rates for channels with memory," *IEEE Trans. Inf. Theory*, vol. 52, no. 8, pp. 3498–3508, Aug. 2006.
[52] J. Chen, R. M. Tanner, C. Jones, and Y. Li, "Improved min-sum decoding algorithms for irregular LDPC codes," in *Proc. IEEE Int. Symp. Inf. Theory (ISIT)*, Sep. 2005, pp. 449–453.
[53] L. Dai, J. Tan, and H. V. Poor, "Delay-phase precoding for wideband THz massive MIMO," 2021. [Online]. Available: arXiv:2102.05211.
[54] U. Wachsmann, R. F. H. Fischer, and J. B. Huber, "Multilevel codes: Theoretical concepts and practical design rules," *IEEE Trans. Inf. Theory*, vol. 45, no. 5, pp. 1361–1391, Jul. 1999.
[55] G. H. Mealy, "A method for synthesizing sequential circuits," *Bell Syst. Tech. J.*, vol. 34, no. 5, pp. 1045–1079, Sep. 1955.
[56] E. F. Moore, "Gedanken-experiments on sequential machines," *Automata Studies*, vol. 34. Princeton, NJ, USA: Princeton Univ. Press, 1956, pp. 129–153.

PETER NEUHAUS (Graduate Student Member, IEEE) received the B.Sc. degree and the M.Sc. degree (with distinction) in electrical engineering, information technology, and computer engineering from RWTH Aachen University, Germany, in 2014 and 2017, respectively. He is currently pursuing the Ph.D. degree with the Vodafone Chair Mobile Communications Systems, Technische Universität Dresden, Germany. His research interests lie in the areas of signal processing and communications.

MEIK DÖRPINGHAUS (Member, IEEE) received the Dipl.-Ing. degree (with distinction) and the Dr.-Ing. degree (*summa cum laude*) in electrical engineering and information technology from RWTH Aachen University, Aachen, Germany, in 2003 and 2010, respectively. From 2004 to 2010, he was with the Institute for Integrated Signal Processing Systems, RWTH Aachen University. From 2010 to 2013, he was a Postdoctoral Researcher with the Institute for Theoretical Information Technology, RWTH Aachen University. Since 2013, he has been a Research Group Leader with the Vodafone Chair Mobile Communications Systems and the Center for Advancing Electronics Dresden (cfaed), Technische Universität Dresden, Germany. In 2007, he was a visiting researcher at ETH Zürich, Zürich, Switzerland. From 2015 to 2016, he was a Visiting Assistant Professor at Stanford University, Stanford, CA, USA. His research interests are in the areas of communication and information theory. He received the Friedrich-Wilhelm Preis of RWTH Aachen in 2004 and the Siemens Preis in 2004 for an excellent diploma thesis, and the Friedrich-Wilhelm Preis of RWTH Aachen in 2011 for an outstanding Ph.D. thesis. He has coauthored a paper that received a Best Student Paper Award at the IEEE Wireless Communications and Networking Conference 2018.

GERHARD FETTWEIS (Fellow, IEEE) received the Ph.D. degree from RWTH Aachen in 1990, under the supervision of H. Meyr. After one year at IBM Research, San Jose, CA, USA, he moved to TCSI, Inc., Berkeley, CA, USA. He has been Vodafone Chair Professor with TU Dresden since 1994, and heads the Barkhausen Institute since 2018. He coordinates the 5G Lab Germany at TU Dresden. In 2019, he was elected into the DFG Senate. His research focusses on wireless transmission and chip design for wireless/IoT platforms, with 20 companies from Asia/Europe/U.S. sponsoring his research. In Dresden his team has spun-out sixteen start-ups, and setup funded projects in volume of close to EUR 1/2 billion. He co-chairs the IEEE 5G Initiative, and has helped organizing IEEE conferences, most notably as TPC Chair of ICC 2009 and of TTM 2012, and as General Chair of VTC Spring 2013 and DATE 2014. He is a member of the German Academy of Sciences (Leopoldina), the German Academy of Engineering (acatech), and received multiple IEEE recognitions as well as the VDE ring of honor.